

# Supplementary Materials for

# Synaptic architecture of a memory engram in the mouse hippocampus

Marco Uytiepo et al.

Corresponding author: Anton Maximov, amaximov@scripps.edu

Science **387**, eado8316 (2025) DOI: 10.1126/science.ado8316

# The PDF file includes:

Materials and Methods Figs. S1 to S14 References

# Other Supplementary Material for this manuscript includes the following:

MDAR Reproducibility Checklist Data S1 to S5

#### Materials and Methods

# Mouse lines and expression vectors

The  $Fos^{DD-Cre}$  and  $Camk2^{Cre}$  strains used in this study have been described previously (33, 35, 90). Mice were housed, crossed, and analyzed in accordance with protocols approved by the IACUC committee. All animals were a mix of C57BL/6 and 129/SV backgrounds. All studies were performed with heterozygote  $Fos^{DD-Cre}$  mice. Neurons carrying a single copy of this allele exhibited no apparent defects in native Fos expression in vitro and in vivo (fig. S2). Males and females were examined together. The APEX2-mGFP and Cherry-H2B coding sequences were inserted into a well-characterized shuttle vector containing the EF1 $\alpha$  promoter and a DIO cassette for inducibility with Cre (90-92). For constitutive expression of fluorescent proteins, the coding sequences were subcloned into a similar vector containing the pan-neuronal Synapsin (Syn) promoter.

#### **AAV** production and injections

AAVs were generated in house using HEK293T cells, purified by Heparin-based affinity chromatography, titered by real-time quantitative PCR, and injected into the brains of mice carrying the Cre drivers at titers of  $2x10^{12}$  GC/ml, as previously described (90-93). Mice were anesthetized with 1.5%–2% Isoflurane in O<sub>2</sub>; stereotaxic injections were performed bilaterally into the dorsal areas of CA3 and CA1. Viruses were infused for 5 minutes at a rate of 100 nl per minute. Although infection of adjacent CA2 could not be avoided, this did not affect our results, as the axons of CA2 and CA3 neurons innervating the CA1 are largely segregated (94).

# **Drug delivery**

TMP-lactate (Sigma, Cat #T0667) was reconstituted in PBS prior to each experiment (30 mg/ml) and administered to mice by intraperitoneal injections through a 29 g needle at a dose of  $50 \mu g/gm$  body weight.

#### **Neuronal cultures**

Cortices from P0 pups were dissociated using papain and seeded onto 24-well plates coated with poly-D-lysine (Millipore). Cultures were maintained for 1 hour in MEM (Invitrogen) supplemented with fetal bovine serum (Invitrogen) and glucose (Sigma), followed by incubation in serum-free Neurobasal-A (Invitrogen) supplemented with B27 (Invitrogen) and Glutamax (Invitrogen). Cultures were kept at 37°C in humidified incubators with 5% CO2 until use and were immunostained as we have previously described (93).

# Fluorescent imaging of brain sections

Mice were anesthetized with isoflurane and perfused transcardially with 25 ml of ice-cold PBS followed by 25 ml of 4% PFA in PBS, using a peristaltic pump. Brains were removed, incubated overnight in 0.4% PFA, and sliced in ice-cold PBS using a vibratome. 90  $\mu$ m thick DAPI-stained coronal sections were imaged under the Nikon C2 microscope with 0.3-0.5  $\mu$ m Z-intervals using 20x and 40x objectives. Uniform digital manipulations were applied to all images.

#### **Contextual fear conditioning**

Mice were allowed to explore the conditioning chambers (Med Associates SD) for 3 minutes before receiving 4 bursts of foot shocks (0.55 mA, with 1-minute intervals between shocks). Control groups were exposed to the same visual and olfactory stimuli without receiving

foot shocks. Memory retrieval was performed 7 days later by re-exposing the mice to the original context. Freezing behavior was measured in 3-minute intervals with 0.75 second bouts. These tests were conducted with separate cohorts of mice to ensure the proper functioning of the fear-conditioning apparatus and to confirm that newly acquired associative memories were not disrupted during animal housing prior to tissue collection for SBEM. Given the technical challenges of sequentially co-labeling neural ensembles activated during learning and memory recall with two distinct EM-compatible markers, and the evidence suggesting that these ensembles are largely segregated (12), all 3D-EM analyses were conducted without retrieval.

#### **Electrophysiology**

Mice were anesthetized with isoflurane. Brains were removed and placed into an ice-cold oxygenated buffer (95%O2/5%CO2) containing 228 mM sucrose, 2.5 mM KCl, 0.5 mM CaCl<sub>2</sub>, 7 mM MgCl<sub>2</sub>, 26 mM NaHCO<sub>3</sub>, 1 mM NaH<sub>2</sub>PO<sub>4</sub>, and 11 mM glucose. Transverse, 300 μm thick slices were sectioned with a vibratome and initially stored at 32°C in oxygenated artificial cerebrospinal fluid (ACSF) containing 119 mM NaCl, 2.5 mM KCl, 1 mM NaH<sub>2</sub>PO<sub>4</sub>, 26 mM NaHCO<sub>3</sub>, 1.3 mM MgCl<sub>2</sub>, 2.5 mM CaCl<sub>2</sub>, 11 mM glucose (pH 7.4, 292 mOsm), and then allowed to recover for 1 hour in oxygenated ACSF at 24 °C prior to recording. Membrane and synaptic currents were monitored in whole-cell current- and voltage-clamp modes, respectively, using Multiclamp 700B amplifier (Molecular Devices, Inc.). Recordings were performed at room temperature. The pipette solution contained 135 mM CsMeSO<sub>4</sub>, 8 mM CsCl, 0.25 mM EGTA, 10 mM HEPES, 2 mM MgATP, 0.3 mM Na<sub>2</sub>GTP, 5 mM QX-314, and 7 mM Na<sub>2</sub>phosphocreatine (pH 7.4, 302 mOsm). Synaptic responses were evoked by 1 ms local field stimulation using an extracellular electrode. Data were sampled and analyzed with pClamp10 (Molecular Devices, Inc.) and OriginPro (Origin Lab) software packages.

# Sample preparation for EM

Mice were anesthetized via intraperitoneal injections of ketamine/xylazine, followed by transcardial perfusion with oxygenated Ringer's solution. A second perfusion was performed using a buffer containing 2% paraformaldehyde, 2.5% glutaraldehyde, 150 mM cacodylate, and 2 mM CaCl<sub>2</sub>. Brains were post-fixed overnight in the same solution at 4°C. 100 µm thick coronal slices were cut using a vibratome and prepared for SBEM imaging through the following sequential procedures: 1) Overnight post-fixation at 4°C, followed by washes in buffer containing 150 mM cacodylate and 0.2 mM CaCl<sub>2</sub>; 2) Fixation at room temperature for 1 hour in 2% OsO<sub>4</sub> in cacodylate; 3) Staining in 0.5% aqueous thiocarbohydrazide; 4) Staining with 2% aqueous OsO<sub>4</sub>; 5) Overnight incubation at 4°C in 2% aqueous uranyl acetate; 6) Staining with lead aspartate at 60°C for 30 minutes; 7) Dehydration on ice using 70%, 90%, and 100% ethanol, followed by dry acetone; 8) Infiltration with acetone ACM; 9) Embedding in 100% Durcupan resin at 60°C for 48 hours. For steps 2 to 6, each procedure was followed by washes in water at room temperature. Approximately 1 mm² tissue pieces were mounted on Gatan SBEM specimen pins using conductive silver epoxy.

# Acquisition and analysis of 3D-EM datasets

# SBEM imaging

Samples were imaged under the Zeiss Merlin scanning electron microscope equipped with a Gatan 3View. Imaging was performed at 2.5 kV and 85 pA using a focal charge compensation device to minimize specimen charging (2.5x10<sup>-3</sup> mbar nitrogen gas). ~110,000 μm<sup>3</sup> stacks were

collected from the dorsal CA1sr using 15k x 15k raster images with 4 nm pixels, 2 µs pixel dwell time, and 60 nm Z steps. Acquired volumes were aligned in IMOD (41).

# Deep learning-based image segmentation

Automatic segmentation of various subcellular structures was performed using CDeep3M, an image segmentation platform that leverages a convolutional neural network (CNN) (43, 44). This platform effectively processes multiple microscopy modalities, including SBEM. Network training and inference were conducted using the Docker-based version of CDeep3M on both local lab GPUs and Amazon Web Service (AWS). To increase efficiency, instead of training models from scratch, existing neural networks were retrained on the specific SBEM image sets used in this study. This domain adaptation approach reduced effort and time by 90%, while maintaining high segmentation accuracy. Pre-trained models for plasma membranes, mitochondria, vesicles, and synapses were downloaded from the publicly available Cell Image Library and retrained using manually segmented ground truth labels from each image stack. New models for dendritic spine heads, axon terminals, and astrocytes were trained from baseline. Training sessions employed 3D label sizes ranging from 48 to 192 µm<sup>3</sup>, with 45,000 to 70,000 iterations. The automatically segmented data were benchmarked against our manual reconstructions of the same features within a 47 µm<sup>3</sup> volume. We also performed side-by-side comparisons of spine head volumes and spine densities per µm<sup>3</sup>, as measured in our datasets (96 µm<sup>3</sup> and 48,000 µm<sup>3</sup> for manual and CDeep3Massisted reconstructions, respectively), with previously published manual reconstructions of 42– 219 µm<sup>3</sup> 3D-EM stacks from CA1sr (27). All image contrast adjustments and manipulations were performed using Fiji/ImageJ (95). Validated models were applied to automatically segment entire volumes. The output prediction maps were stitched together and used for either fully automated reconstruction in IMOD or semi-automated reconstructions in VAST (20). For modeling the gross anatomy of neurites in the block, instance segmentation was performed using PyTorch Connectomics, a recently developed deep learning framework for automatic and semi-automatic annotation of connectomics datasets (42). The CNN was trained with image stacks in which all neurites and astrocytes were segmented. The trained network was used to predict an affinity map and a watershed algorithm was used to generate the dense segmentation. The automatic reconstructions from this pipeline were then used for 3D visualization.

#### Automatic reconstructions

Automated reconstructions were performed using IMOD and PyIMOD, a python library for manipulating IMOD files (https://github.com/CRBS/PyIMOD). Prediction maps of dendritic spine heads, axon terminals, synapses, vesicles, mitochondria, and astrocytes were initially generated in CDeep3M. Since each SBEM image set had slight variations in XY dimensions, cropped versions of the prediction maps were created, with dimensions of ~10,000 x 10,000 pixels across 500 Z-slices (48,000 µm³). Vesicle analysis was restricted to a smaller volume (~12,000 µm³) due to the computational load. 2D contours for each feature were generated using *Imodauto* with thresholding, and small contour artifacts were automatically removed by defining a minimum area. 3D meshes for each object (except vesicles) were created using *Imodmesh*; objects were sorted into separate categories with *Imodsortsurf*. For final post-processing, PyIMOD was employed to remove clipped objects touching the image set border (using *RemoveBorderObjects*) and to filter by contour number, specifying a minimum and maximum slice count (*FilterByNContours*). Volumes and counts for each object per block volume were extracted with *Imodinfo*. To obtain vesicle counts per terminal, the generated vesicle contour

and the final sorted axon terminal files were converted into TIFF format and imported into VAST using the *Import Segmentation from Images* function. Vesicle coordinates were extracted with the Vasttools *Export Particle Clouds* function. Due to the larger Z-step size (60 nm) of the image stacks compared to the vesicle diameters (~40 nm), each 2D contour on a separate slice was considered a unique vesicle. A custom MATLAB script was developed to count the number of vesicles per terminal by checking whether vesicle contour coordinates overlapped with a segmented terminal of a specific ID. Although the automated segmentation approach could introduce merge errors between closely located objects, we reasoned that this would not bias the results, as the same thresholding and filtering criteria were applied uniformly across all experimental conditions. The accuracy of the pipeline was further validated by comparing small-scale automatic reconstructions with manual and instance-based segmentations of the same samples. We found only minimal feature merging, with no systematic bias across different samples.

#### Semi-automatic segmentation

Semi-automatic segmentations were performed using VAST Lite version 1.4.1, a voxel-painting program designed for the analysis of large volumetric datasets (96). We used masked painting in VAST in combination with the CDeep3M predicted boundary maps to constrain painted areas so that the outline of each object is traced automatically. This approach enabled rapid and accurate reconstructions of axons, dendrites, synapses, and mitochondria. Errors arising from occasionally inaccurate boundary predictions were manually corrected. For dendrite and axon segmentation, membrane prediction boundary maps were used to fill the outlines of cellular structures. For mitochondria segmentation, a specific prediction map was applied for masked painting, ensuring the complete filling of each mitochondrial structure. Since this study focuses on excitatory circuits, the analysis was limited to spiny apical dendritic segments of PNs and axons that form glutamatergic synapses, as characterized by the presence of PSDs. All segmented volume data were extracted using VastTools in MATLAB for further analysis.

# <u>Skeletonization and assignment of coordinates</u>

Skeletons for traced dendritic and axonal segments were generated using VAST. The *Annotation* function was employed to place connected nodes along the centerline of each reconstructed structure's cross-section, spanning from the first to the last slice of the image volume, at regular intervals. Image stacks containing dendritic spines or axonal terminals along the skeletonized length were marked to assess the distribution and distances of spines and terminals across the entire structure. In axons, nodes were placed in the inter-terminal spaces to account for the inherent curvature of the axons. In instances where an axon split to form a new branch, a single path was reconstructed to ensure compatibility with the majority of the dataset. Annotated length data were extracted using VastTools.

#### Reporter tracing

Projections and synapses were categorized as APEX2-mGFP positive (+) or negative (-) through manual tracing of the reporter in pre-processed SBEM datasets. This strategy was employed due to concerns that the variability in peroxidase staining intensity across morphologically diverse structures of different sizes could reduce the accuracy of automatic detection. (+) axons and dendrites were identified by the presence of dark staining throughout their membranes, with intensified staining in smaller compartments serving as a clear indicator of

reporter expression. Axonal fibers exhibited notably stronger staining than dendrites, occasionally obscuring intracellular contents. However, this did not hinder the assessment of synapse distributions, and all reconstructed excitatory axons were included in the analysis. For mitochondrial localization within terminals, a few axons with staining too dark for segmentation were omitted. Staining intensity was comparable across blocks, with no significant difference in the fraction of excluded axons between samples. While the CNN models were trained on these image sets, prediction errors for labeled structures were more frequent due to the dark staining, thus corrections were made manually. Although slight differences in volume measurements between (+) and (-) structures may have arisen due to segmentation variations, virtually all documented morphological changes in (+) PNs of fear-conditioned mice were absent in mice exposed to neutral CS. Therefore, any potential differences in absolute volumes were not significant enough to affect the overall results.

# *Reconstruction of (+) and (-) structures*

We reconstructed sets of (+) and randomly selected adjacent (-) dendrites with similar orientations. While the large apical dendritic trunks were present in the CA1sr, we focused on smaller, higher-order branches, which formed the majority of dendritic spines. The shaft diameters of selected dendrite pairs were matched, with only minimal variation observed across the entire set. To further reduce variability, spine measurements were performed on shorter segments (~100 spines per branch). Axons were chosen based on the same criteria and were reconstructed throughout the block. Some spine-innervating axons formed at least one synapse with smooth, non-spiny dendrites, and there were occasional synapses onto dendritic shafts. These synapses were included in the synapse distribution measurements along axonal shafts but were excluded from volumetric measurements.

#### *Justification for excluding interneurons*

Consistent with previous studies demonstrating that Fos and other immediate early genes are expressed in GABAergic interneurons (77, 93, 97), we also observed labeling of putative inhibitory neuronal structures that formed symmetrical, shaft-targeted synapses. While intriguing, these reconstructions were excluded from the final quantifications. We reasoned that an in-depth analysis of inhibitory components of an engram goes beyond the scope of the present study, as there is still limited understanding of the morphological hallmarks of synapses from the diverse interneuron subtypes (77) that innervate PNs and other interneurons in different hippocampal subfields, including CA1sr.

# Classification of Terminals and Spines

Nerve terminals were classified based on the number of innervated spines as either SSBs (1 spine) or MSBs (2+ spines). Due to the large distances typically separating presynaptic boutons along the axon, there was little ambiguity regarding which bouton a spine belonged to. Additionally, presynaptic and postsynaptic partners were identified by the presence of visible PSDs. In cases where the distinction between MSBs and SSBs was unclear due to irregular shapes, the continuity of the vesicle pool was used to define the terminal borders. Dendritic spines were classified into five morphologically distinct types: Mushroom (M), Thin (T), Stubby (S), Filopodia (F), and Bifurcated (B) as described previously (44, 98). Rare spines with unclear shapes were excluded from quantifications, except for measurements of distances between synapses.

# Splitting of spine heads and terminals

Spine heads and nerve terminals were manually separated from their parent structures using the *Splitting* tool in VAST. This process created new segments, which were then automatically volume-filled using the *Filling* tool. Spine heads were split at the base of the neck for clear delineation. For synapse analysis along projections, a few synapses were observed forming onto non-spiny, smooth dendrites and dendritic shafts. These constituted a small fraction of the total synapse pool and were excluded from volumetric measurements. Terminals were split at points where axonal cross-sections minimized, vesicle pools ended, or opposing PSDs terminated.

# PSD, ASI and ATI measurements

PSDs were identified as darkly stained regions at the ends of dendritic spines, typically positioned opposite axonal terminals containing synaptic vesicles. PSDs were segmented in VAST by adjusting the pen size according to PSD thickness. Given that the visibility of the PSD can vary depending on the spine's orientation (e.g., cross-sectioned synapses may appear more continuous than oblique synapses), PSD volumes may have been underestimated in a few cases. However, this variability was unlikely to introduce significant bias, as the same segmentation criteria were applied consistently across all conditions, and large sample sizes were analyzed. Axon/spine and astrocyte/terminal interfaces (ASIs and ATIs) were defined as the entire contact area between the axon terminal and the postsynaptic spine or astrocyte. ASIs and ATIs were segmented in VAST using a fixed pen size across each plane of the synapse, except in the case of oblique synapses, where the entire contact zone was filled in the plane. Similar to PSD measurements, the same rationale applies for potential underestimation of ASI/ATI volumes due to synapse orientation.

#### Mitochondria and SA

Mitochondria-positive terminals were identified by the presence of one or more mitochondria within the boundaries of the bouton, following the criteria described above. Mitochondria were semi-automatically segmented in VAST using masked painting with a CDeep3M mitochondria prediction map. In cases where the prediction map contained errors, mitochondria were manually corrected or traced. Despite the dark staining of presynaptic compartments in (+) PNs, mitochondrial boundaries typically remained clearly distinguishable. Only a few (+) axons, in which all intracellular contents were obscured, were excluded from analysis. Spines were classified as SA-positive when stacks of SER folds were visible in their necks and/or heads. This population was distinguished from spines containing only a single tubular SER.

#### Data extraction and analysis

Large-scale automated reconstructions generated in IMOD were extracted in a Linux terminal using *Imodinfo* and saved as .csv files for analysis. This method was used to calculate the cubic density of spine heads, terminals, mitochondria, and vesicles. All other data extractions, including volume measurements, coordinates for length and distance measurements, and 3D surface meshes, were performed using VastTools in MATLAB. Uniform parameters were applied to all samples for data extraction and 3D model exports. Since VastTools allows quantification at lower resolutions, we used the native voxel size of the image stacks (4 nm x 4 nm x 60 nm) at Mipmap level 0. All numerical data were extracted prior to 3D modeling.

# Volume measurements and 3D model extraction

The volumes of dendritic spine heads, axonal terminals, PSDs, ASIs, ATIs, and mitochondria were measured using the *Measure Segment Volume* function, which calculates the total number of voxels for specified objects within a defined boundary. 3D models were generated using the *Export 3D Models* function, which creates surface meshes in VAST and exports them as .obj files for further modeling in Blender. To facilitate post-export smoothing, some features were exported as lower-resolution models (Mip 2-3). The *Export Particle Clouds* function was used to export 3D surface mesh models of vesicles (.obj files) for 3D modeling in Blender.

#### Coordinate exporting

Whole skeleton length measurements were extracted using the VastTools function Measure Skeleton Lengths, which sums the distances between nodes placed along neurites. Since internode length measurement functions are not available in the current version of VastTools, we developed custom MATLAB scripts that utilized API to extract these measurements. As mentioned above, skeleton nodes were placed along neuropil structures (e.g., axons) using the Annotation tool in VAST. To prevent overestimation of length, nodes were placed at the center of each structure. For dendrite analysis, nodes were positioned at the start and end of dendritic fragments, as well as at branching points where spines extended from the shaft. This allowed us to extract parameters such as dendritic fragment length, linear spine density, and distances between individual spines. Every dendritic protrusion was considered a spine. While the skeletonization approach for dendrites was also applied to axonal fibers, we accounted for the higher curvature of these structures by placing nodes at the beginning and end of each axon, in terminals contacting spines, and at intervals along the fibers to match their curvature. By flagging nodes corresponding to axonal terminals, we could accurately calculate axon length, terminal density, and distances between terminals. Rare axonal fibers innervating dendritic shafts were excluded from analysis, as they were presumed to be from interneurons. The exact coordinates of the nodes were extracted using the VAST API function Getannoobject, which outputs a matrix containing the x, y, and z coordinates of every node. We then designed MATLAB scripts to compute distances based on the All distance and length measurements were type of analysis. calculated using the MATLAB function *Vecnorm*, computes which the Euclidean norm, where vector v with N elements is defined as:

$$||v|| = \sqrt{\sum_{k=1}^{N} |v_k|^2}$$

#### 3D Modeling

Final 3D modeling was conducted either in the VAST 3D viewer or in Blender 3.5 (Blender.org), an open-source 3D computer graphics software with robust modeling, material editing, and rendering capabilities. The VAST 3D viewer was primarily used for visualizing the raw EM block and large-scale reconstructions of axons and dendrites by combining CDeep3M and PyTorch Connectomics prediction maps with VAST's Segmentation import functions. All other modeling was completed in Blender. First, 3D surface meshes of

neuropil structures were imported as .obj files without any post-import size scaling. To reduce computational load, most features were exported at a lower resolution (Mipmap level 2-3), while still maintaining their native scale. Importing .obj models from VastTools also preserved the spatial location of each segmented feature, ensuring that the actual spatial distribution from the SBEM image stack remained intact. Synaptic vesicles were represented using pre-made 40 nm 3D models included with VastTools. Smoothing, color enhancements, and material assignments were applied equally across all conditions and brains. Color-coding and patterning schemes for each feature are described in the figure legends. Except for vesicles, all structures were smoothened using the *Smooth vertices* function in Blender. Final scenes were rendered using the *Cycles Renderer*.

# **Data blinding**

To ensure consistency in annotations and eliminate potential bias, manual tracing of all subcellular structures, as well as classification and extraction of various synaptic parameters, were conducted by multiple trained investigators who were blinded to the experimental conditions.

#### **Quantifications and statistics**

All final quantifications, curve fittings, and statistical analyses were performed using Origin Pro. Most measured parameters, such as terminal-to-spine distances and the sizes of various structures within individual synapses, deviated significantly from a normal distribution. Therefore, non-parametric statistical tests were employed throughout much of the study. Standard comparisons of populations were assessed using Mann-Whitney U Test or Kruskal-Wallis ANOVA. For datasets where the Kruskal-Wallis ANOVA indicated a significant group effect, post-hoc analyses were performed using Dunn's test to compare individual groups. For comparison of mice (box with data overlap plots), p values were determined by t-test with Welch correction. Correlation analyses were performed using either Spearman or Pearson tests, depending on the dataset. Differences between Spearman correlation coefficients were statistically evaluated using the Fisher transformation test. For correlation analyses where Pearson's correlation coefficient was calculated, we employed a weighted linear regression approach to account for varying precision across data points. Each data point was assigned a weight equal to the inverse of the square of its standard error. The decision to use the Lognormal probability density function (PDF) (99) for analyzing distributions was based on a systematic side-by-side comparison of each dataset with Gaussian, Exponential, Weibull, Lognormal, and Gamma fitting functions, along with a Kolmogorov-Smirnov test for goodness-of-fit. These analyses indicated that the Lognormal PDF was the most versatile fit for our data, with the exception of the ATI data where Exponential fits were more appropriate.

The PDF of a lognormal distribution is:

$$y = f(x \mid \mu, \sigma) = \frac{1}{x\sigma\sqrt{2\pi}} \exp\left(\frac{-(\log x - \mu)^2}{2\sigma^2}\right), \quad for \, x > 0.$$

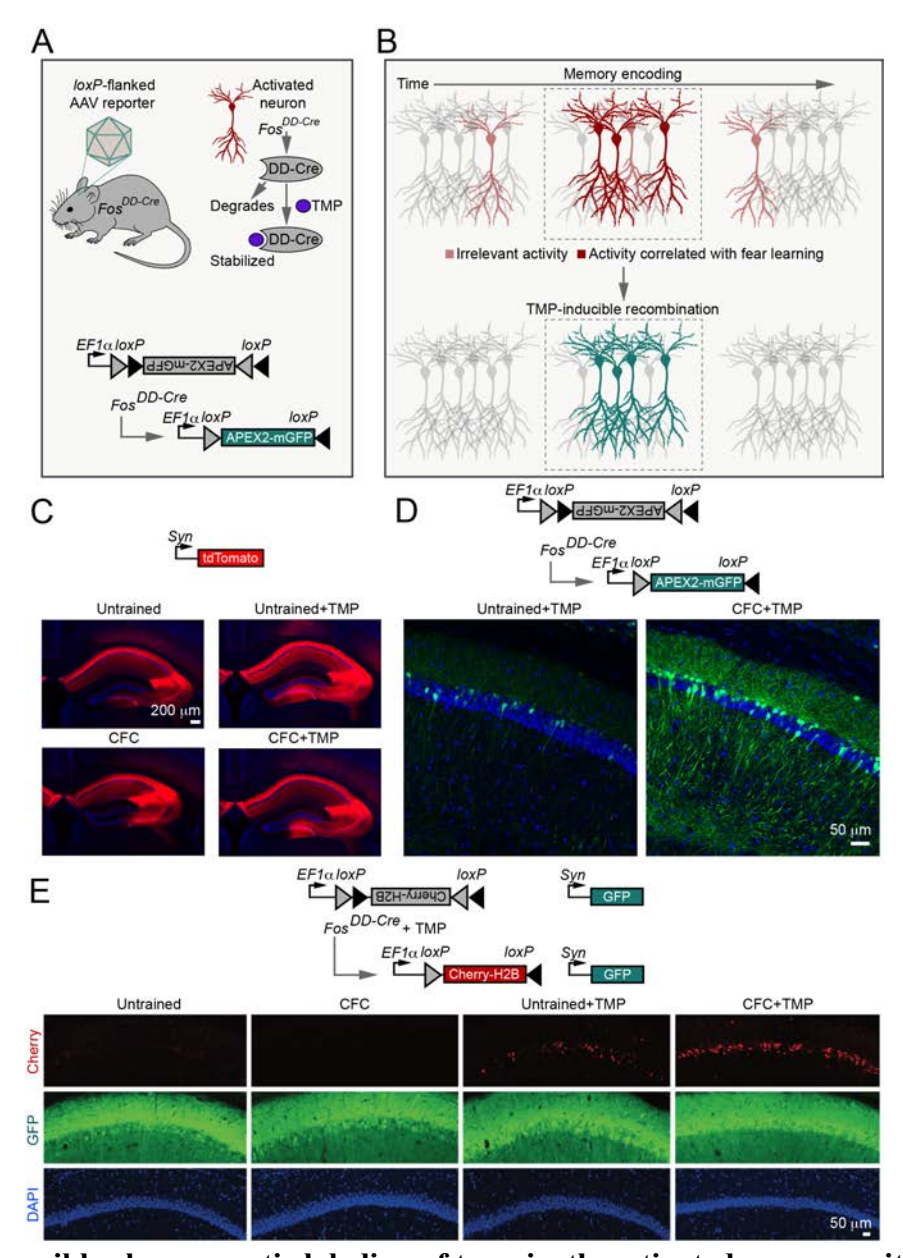


Fig. S1. Irreversible chemogenetic labeling of transiently activated neurons with  $Fos^{DD-Cre}$ . (A) Schematic showing viral delivery of loxP-flanked reporters into the brains of  $Fos^{DD-Cre}$  knock-in mice, TMP-

inducible stabilization of DD-Cre in *Fos*-positive neurons, and the DIO:APEX2-mGFP adeno-associated virus (AAV) used for reconstructions. (**B**) Acute induction of viral reporters with TMP in neurons recruited for memory acquisition. (**C** and **D**) *Fos*<sup>DD-Cre</sup> mice were co-injected into areas CA3 and CA1 with AAVs encoding DIO:APEX2-mGFP and tdTomato, driven by the constitutive Synapsin promoter. (**C**) Low-magnification images of tdTomato fluorescence demonstrate consistent virus targeting in the hippocampus under different conditions used for the quantifications presented in Fig. 1E. (**D**) Examples of APEX2-GFP expression in the CA1 of untrained and fear-conditioned mice. (**E**) Additional controls show that sparse, experience-dependent labeling of cellular ensembles in *Fos*<sup>DD-Cre</sup> mice does not reflect poor virus penetrance or recombination efficiency. Mice were injected with two AAVs expressing Cherry-H2B and GFP in a Cre-inducible and constitutive manner, respectively. Note that Cherry-positive cells are detected only after TMP treatment, with an increased number following CFC, while the constitutive expression of GFP under the Synapsin (Syn) promoter is widespread in all experimental settings. In all experiments, single doses of TMP (50 µg/g body weight) or control vehicle solution were administered intraperitoneally 30 minutes post-training.

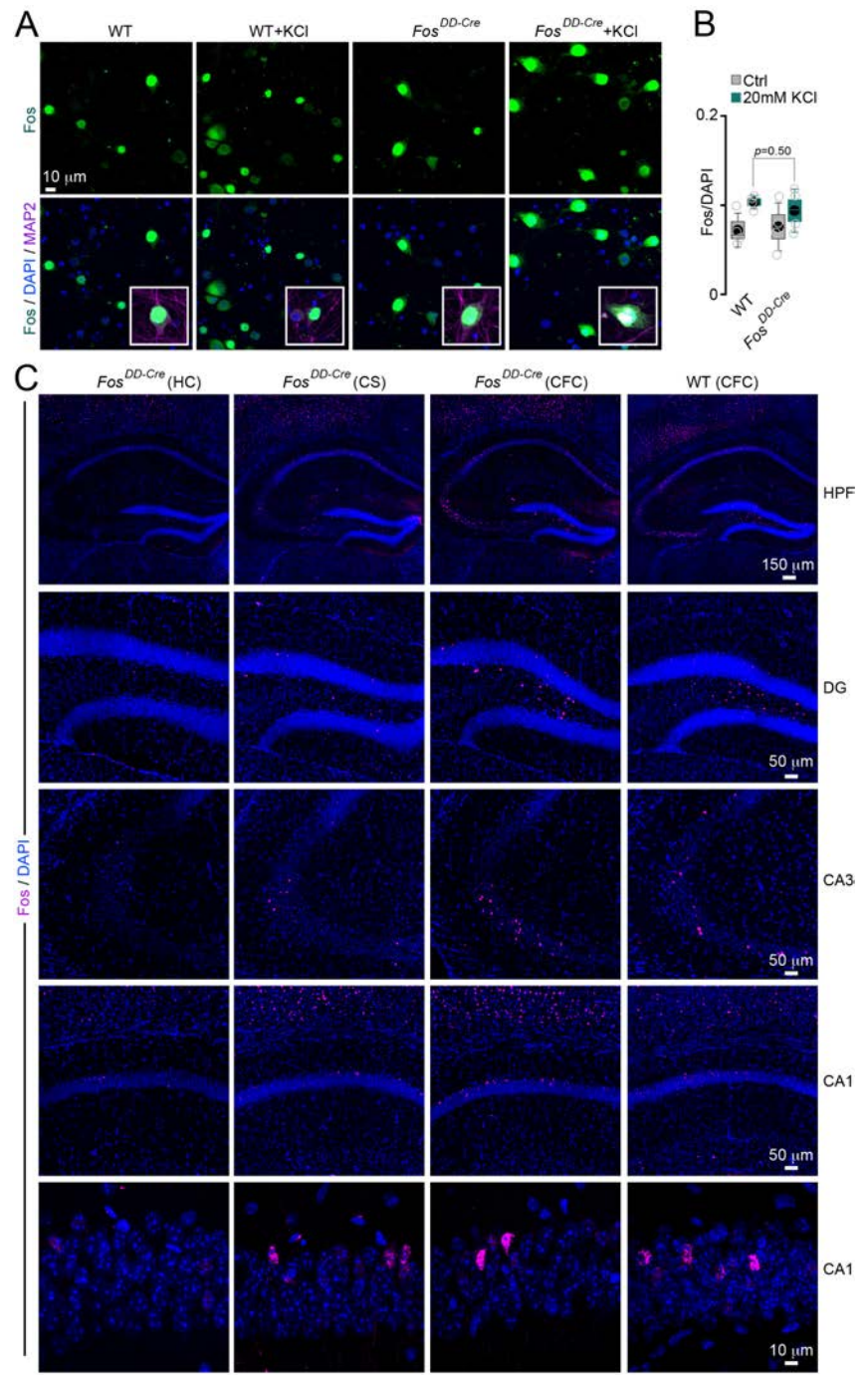


Fig. S2. Expression of native Fos in neurons carrying a single Fos<sup>DD-Cre</sup> allele.

(A and B) Neurons were isolated from the cortices of wild-type (WT) or heterozygous  $Fos^{DD-Cre}$  knock-in mice and maintained *in vitro* for 14 days. Cultures were then immunostained with an antibody against Fos under control conditions or after 10 minutes of depolarization with 20 mM KCl. (A) Typical images of Fos immunofluorescence in DAPI-stained samples. Insets show co-labeling for Fos and the pan-neuronal marker, MAP2. (B) Fractions of Fos-positive neurons in unstimulated and stimulated cultures (n = 4/group). Note that the induction of Fos in the absence of KCl treatment reflects typically high spontaneous network activity in cortical cultures. (C) Images of Fos immunofluorescence in brain sections from heterozygous  $Fos^{DD-Cre}$  and WT mice. Staining was performed either without behavioral conditioning (HC – home cage) or 1 hour after exposure to a conditioned stimulus (CS) or contextual fear conditioning (CFC). Scale bars apply to all panels displaying each brain region.

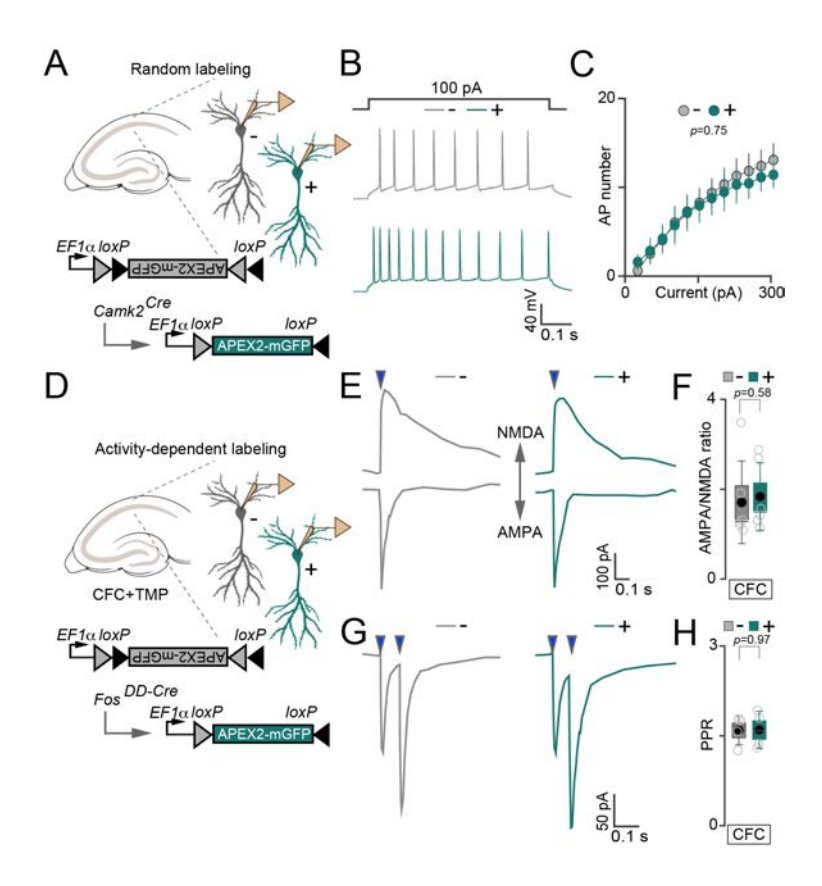


Fig. S3. Electrophysiological analyses of neuronal excitability and synaptic strength.

(A to C) Control experiments showing that the altered electrical properties of PNs with a remote history of activity during associative learning (as summarized in main Fig. 1, F to 1H) are not due to the expression of APEX2-mGFP per se. (A) Schematic of side-by-side whole-cell recordings from randomly labeled and neighboring unlabeled CA1 PNs in acute hippocampal slices. Random labeling was achieved by injecting a diluted virus into the hippocampus of constitutive Camk2<sup>Cre</sup> driver mice, which mediates recombination in all mature glutamatergic neurons. (B) Sample traces of action potentials (APs) evoked by a 100 pA current injection. (C) Number of APs (Mean ± S.E.M.) plotted relative to stimulus intensity. n = 3 mice/7 neurons per group. (**D** to **H**) Synaptic properties of CA1 PNs were assessed 7 days after experience-dependent labeling. (D) Schematic of side-by-side whole-cell recordings from Fos/APEX2mGFP-negative (-) and positive (+) cells in acute hippocampal slices from fear-conditioned, TMP-treated Fos<sup>DD-Cre</sup> mice. (E and F) PNs with a remote history of activity during associative learning do not exhibit widespread changes in synaptic strength. Panels show sample traces of evoked AMPA- and NMDA-type excitatory postsynaptic currents (E, blue arrows indicate the times of 1 ms electrical stimulation through a local extracellular electrode) and quantifications of AMPA/NMDA ratios (F). n = 3 mice/6 neurons per group. In (F) and subsequent similar panels, graphs display individual data points (open circles), mean values (filled circles), standard errors (boxes), standard deviations (vertical whiskers), and medians (horizontal lines). p values were determined by t-tests. (G and H) PNs with a remote history of activity during associative learning do not exhibit widespread changes in presynaptic release probability. Panels show sample traces of AMPA-type currents evoked by two closely spaced 1 ms stimuli (G) and quantifications of paired pulse EPSC ratios (PPR). n = 2 mice/4 neurons per group. In panels (E) and (G), scale bars apply to all traces.

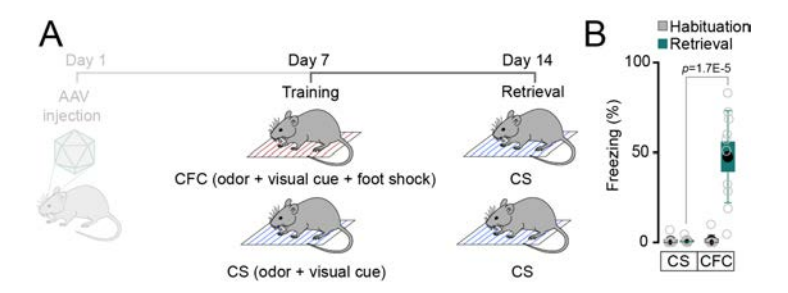


Fig. S4. Fear-conditioned mice retained stable memory at the time of tissue collection for SBEM.

(A) Experimental design. Mice were subjected to CFC or a neutral CS and then re-tested in the original context 7 days later. (B) Quantification of freezing behavior before (habituation) and 7 days after training. n = 10 mice per group. p value was calculated by t-test.

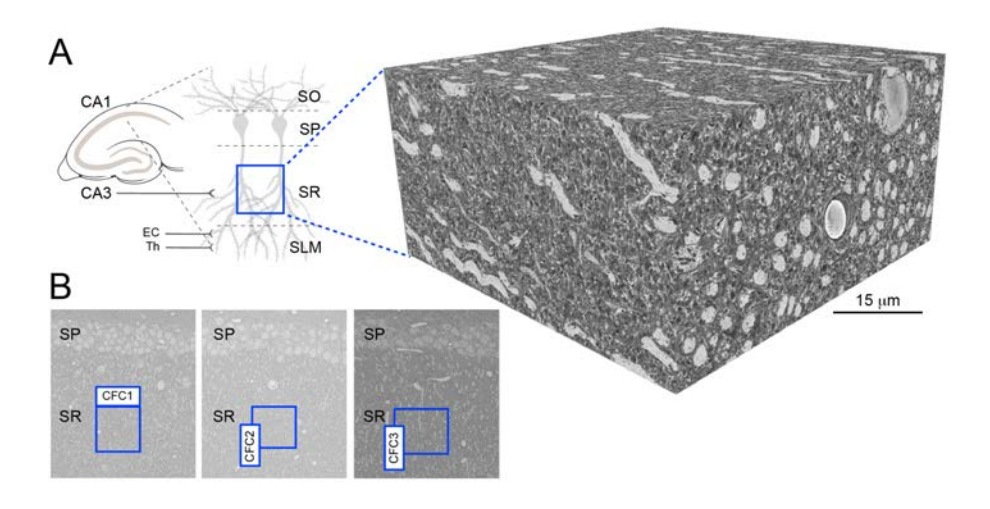


Fig. S5. Examples of raw SBEM data.

(A) Schematic of excitatory pathways in the CA1 region and a typical 3D-EM stack collected from the area of the stratum radiatum (SR) marked by a blue box. (B) Original 2D EM images with actual coordinates of 3D stacks acquired from three different fear-conditioned mice (blue boxes).

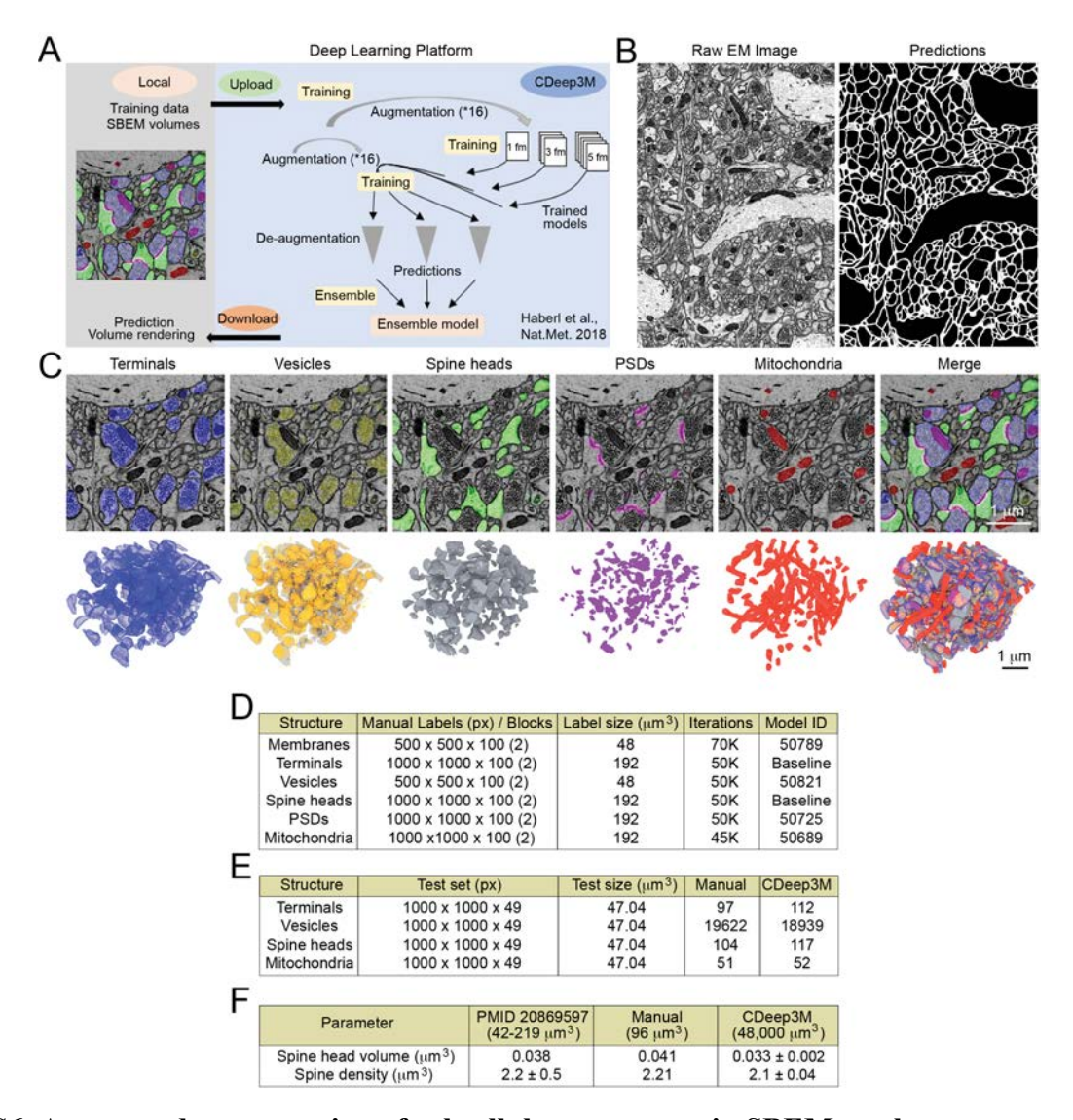


Fig. S6. Automated segmentation of subcellular structures in SBEM stacks.

(A) Workflow for image segmentation using the cloud-based machine learning platform, CDeep3M. (B) Example of automatically segmented plasma membranes. (C) Examples of automatically segmented presynaptic terminals, neurotransmitter vesicles, dendritic spines, postsynaptic densities (PSDs), and mitochondria. For each structure, both the original 2D EM images with color-coded templates and the resulting 3D reconstructions are shown. Scale bars apply to all panels. (D) Network training parameters for segmentation of the indicated structures. (E and F) Examples of benchmarking CDeep3M performance. (E) Number of different structures identified manually or with CDeep3M in the same 3D-EM test sets. (F) Comparisons of spine head volumes and spine densities, showing manual measurements from the rodent CA1 (from an independent study, Mishchenko et al., PMID: 20869597) alongside manual and automatic measurements from the current datasets.

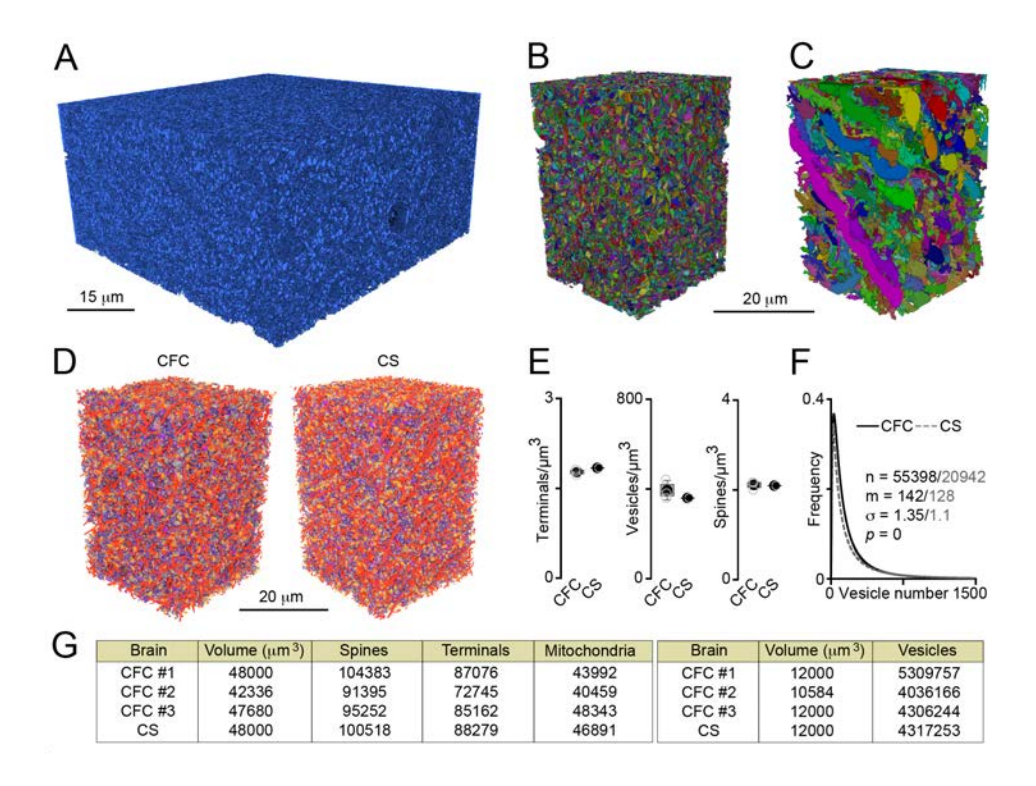
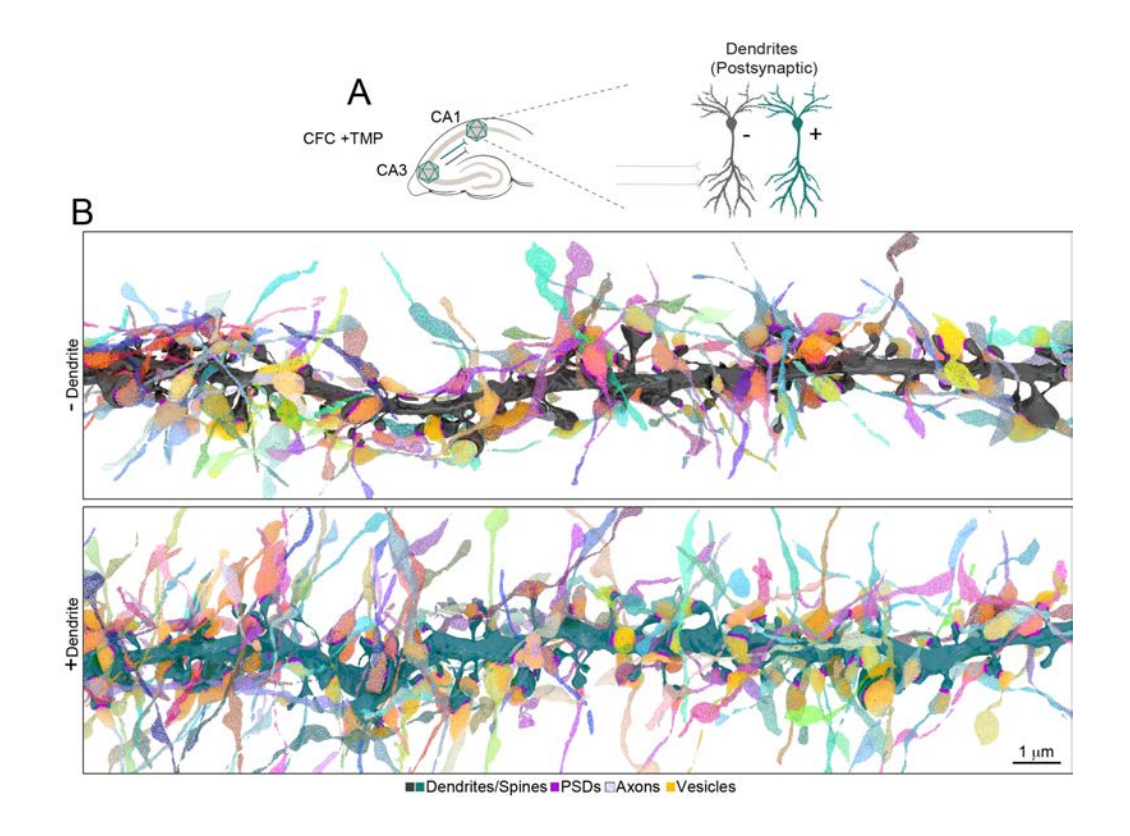


Fig. S7. Examples of annotated SBEM stacks with basic quantifications.

(A) Saturated reconstructions of axons and presynaptic terminals in the entire volume. (B and C) Saturated reconstructions of axons with presynaptic terminals (B) and dendrites (C) in  $\sim 1/9^{th}$  of the total 3D volume. Individual projections are displayed in different colors. Scale bar applies to both panels. (D) Reconstructions of all synapses and mitochondria in volumes acquired from mice subjected to CFC or CS. Structures are color-coded as shown in fig. S6C. Scale bar applies to both images. (E) Averaged counts of terminals, vesicles, and spines per  $\mu$ m<sup>3</sup>, as assessed in difference mice. (F) Distributions of vesicle counts in individual synapses, with lognormal curves and fitting parameters shown. n - sample sizes; m - medians;  $\sigma$  - standard deviations of logarithmic values. (G) Raw values for the indicated parameters, as assessed in partial volumes.



**Fig. S8.** Examples of local connectomes of PNs in the CA1sr of fear-conditioned mice. (A) Schematic of experience-dependent labeling. (B) Reconstructions of dendritic branches of Fos/APEX2-mGFP-negative (-) and positive (+) PNs, along with fibers and terminals of all incoming SchC axons, displayed in different colors. Scale bar applies to both images.

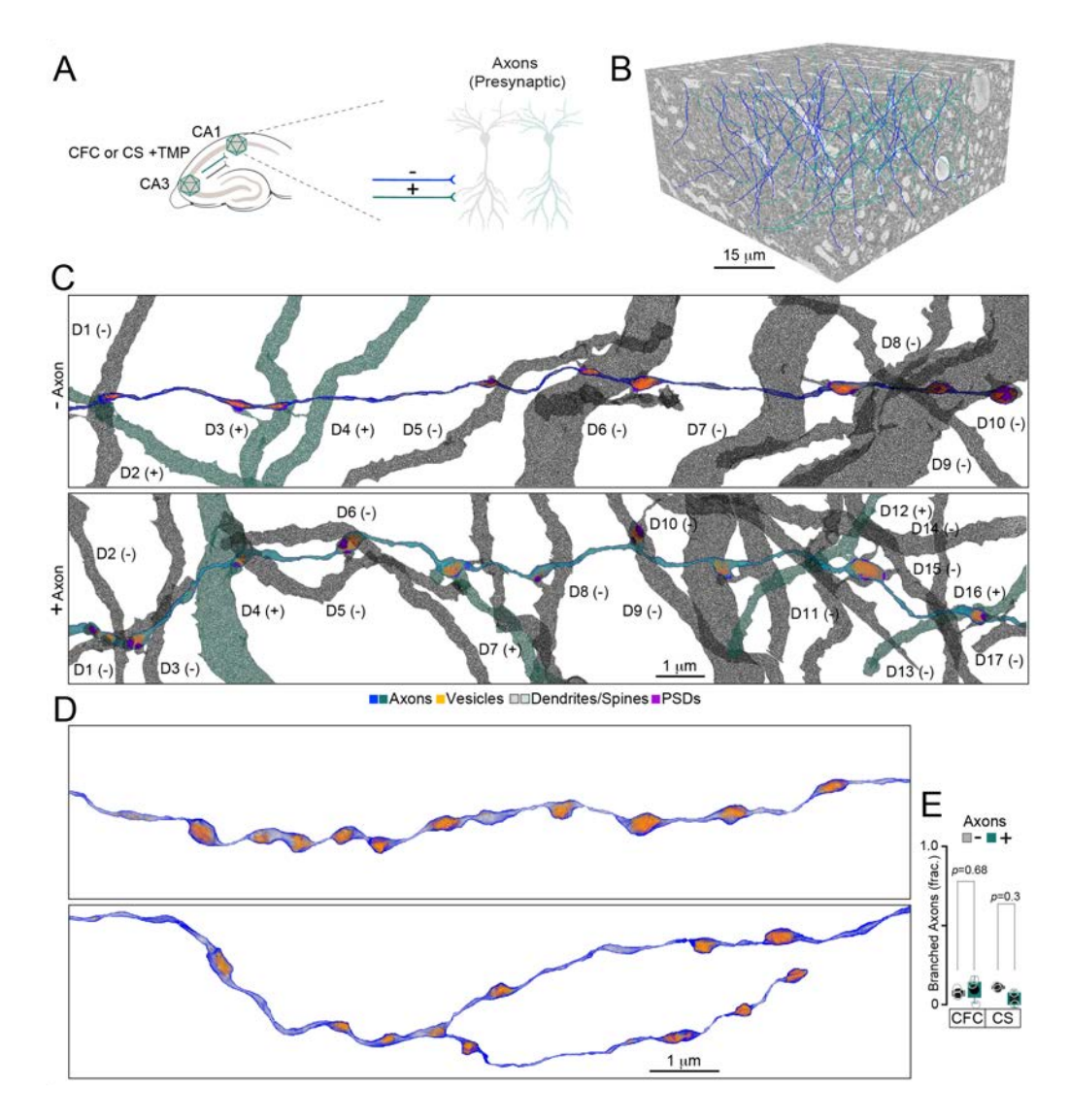


Fig. S9. Analysis of axonal wiring in the CA1sr of mice subjected to CFC or CS.

(A) Schematic of experience-dependent labeling and data categorization. (B) Typical examples of reconstructed Fos/APEX2-mGFP-negative (-) and positive (+) SchC axons in a full SBEM stack. Only a few unlabeled fibers are displayed. (C) Reconstructions of SchC axons terminating in the CA1sr. Different dendrites (marked as D) of CA1 neurons are numbered and color-coded based on activity history. Scale bar applies to both images. (D) Examples of unbranched and branched axons. Scale bar applies to both images. (E) Fractions of branched axons for the indicated experimental conditions, assessed in different mice. CFC, n = 3 mice; CS, n = 2. p values were calculated using t-tests with Welch correction.

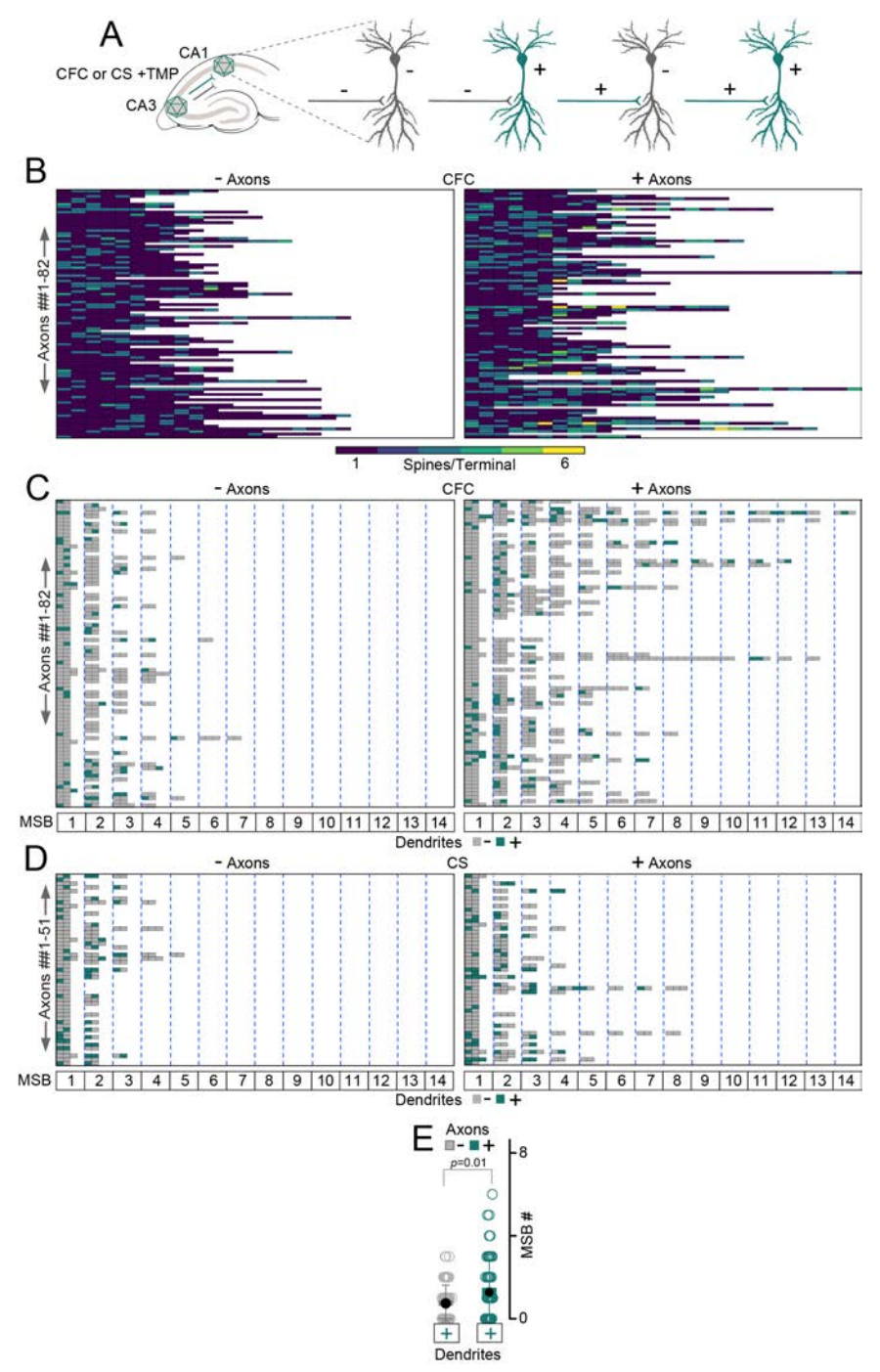


Fig. S10. Analysis of axonal wiring through MSBs.

(A) Schematic of experience-dependent labeling and data categorization. (B) Heatmaps representing the numbers of spines innervated by each terminal of individual Fos/APEX2-mGFP-negative (-) and positive (+) SchC axon in the CA1sr of fear-conditioned mice (n = 3). (C and D) Heatmaps representing axonal wiring via MSBs in the CA1sr of mice subjected to CFC (C, n = 3) or CS alone (D, n = 2). Each box in the vertical columns shows the numbers of color-coded postsynaptic counterparts of each MSB formed by individual Fos/APEX2-mGFP-negative (-) and positive (+) SchC axons (horizontal rows, SSBs are omitted). (E) Cumulative counts of MSBs of (-) and (+) axons terminating onto (+) dendrites of previously activated CA1 PNs in fear-conditioned mice. p value was calculated using a t-test with Welch correction.

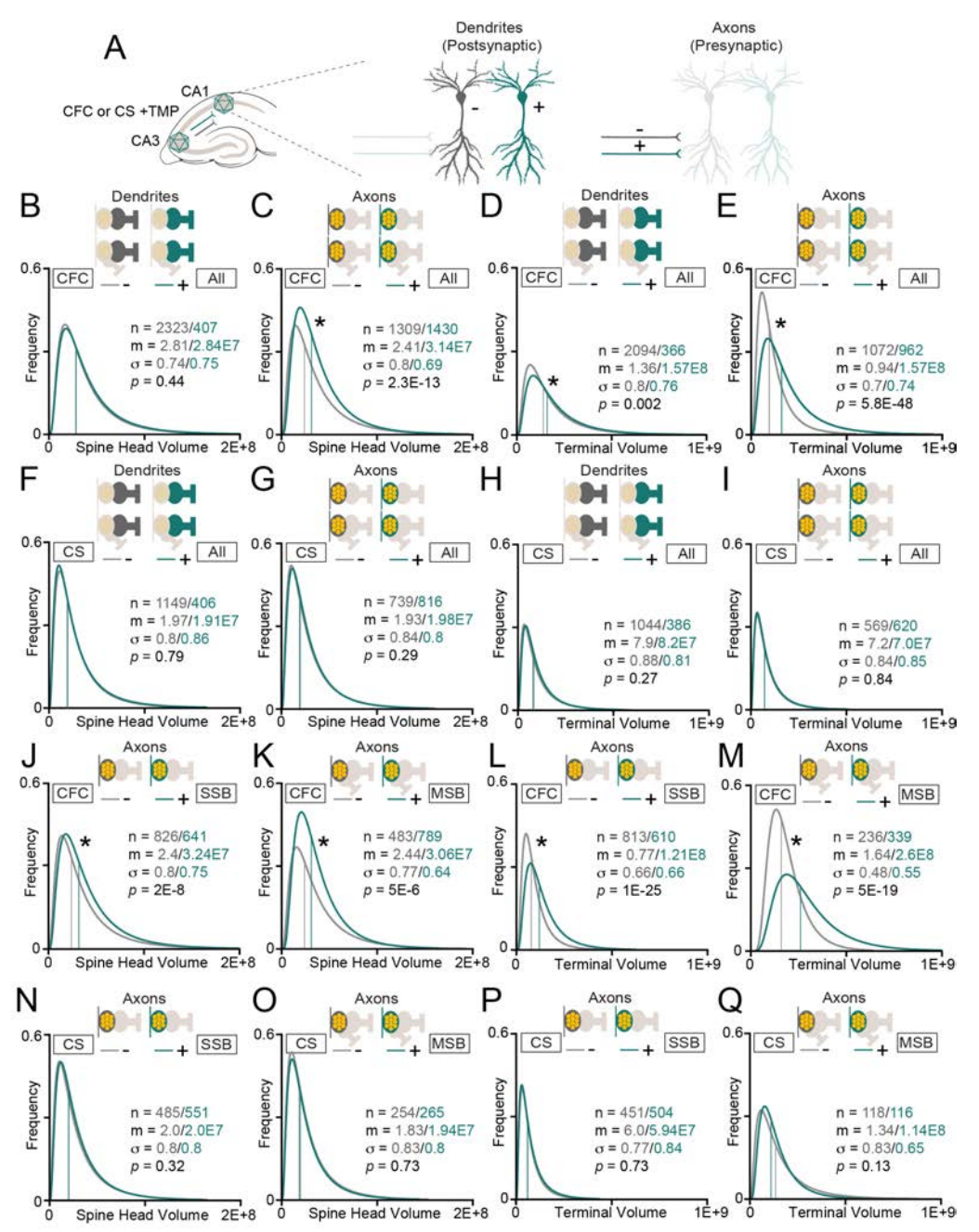


Fig. S11. Distributions of terminal and spine head volumes.

The sizes of individual excitatory synapses formed by PNs with remote histories of activity correlated with fear learning (n = 3 mice) or exposure to a neutral CS (n = 2) were measured in the CA1sr using Fos/APEX2-mGFP labeling on either post- (CA1 dendrites) or presynaptic side (SchC axons) as a frame of reference. (A) Schematic of experience-dependent labeling. (B to Q) Distributions of spine head and terminal volumes. Each panel shows lognormal curves with fitting parameters. n - sample sizes; m - medians;  $\sigma$  - standard deviations of logarithmic values. Datasets are categorized as shown in the legends. (B to E) Synapse sizes in fear-conditioned mice. (B) Spine volumes of (-) and (+) CA1 PNs, measured irrespective of axonal labeling. (C) Spines innervated by (-) and (+) CA3 PNs, measured irrespective of postsynaptic labeling. (D) Terminals innervating (-) and (+) CA1 PNs (postsynaptic label only). (E) Terminals of (-) and (+) CA3 PNs (presynaptic label only). (F to I) Same analyses as in (B to E) were performed in mice subjected to CS. (J to Q) Synapses were further subdivided as SSBs and MSBs. (J to M) Spine head and terminal volumes in mice subjected to CFC. (N to Q) Spine head and terminal volumes in mice subjected to CS. All volumetric measurements are displayed in nm³. p values were calculated using Mann-Whitney tests.

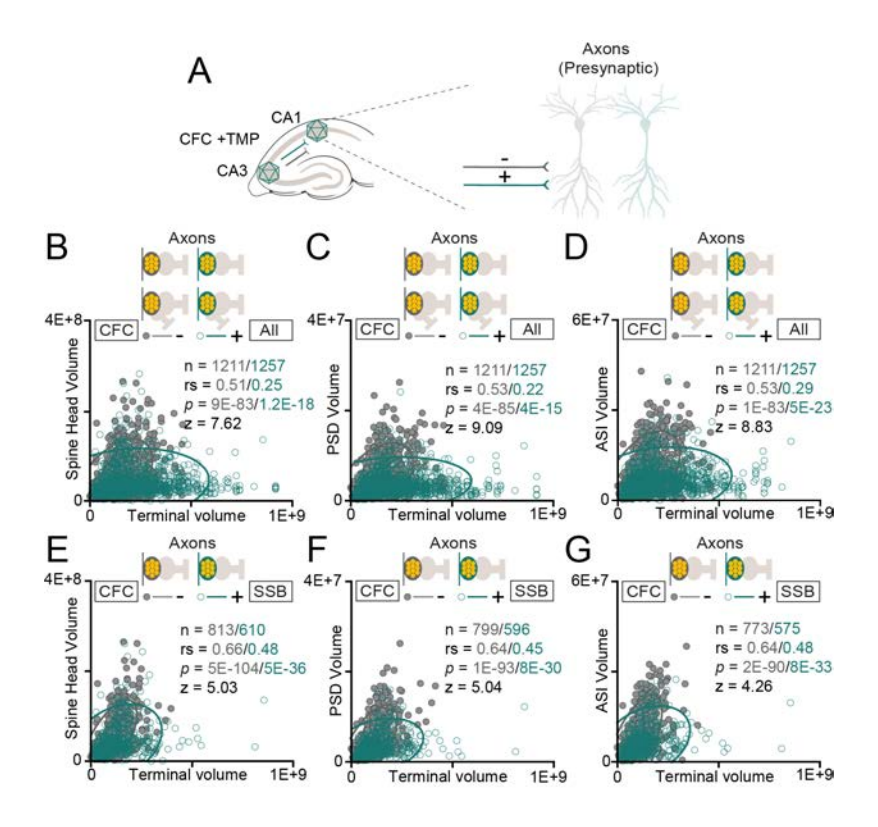


Fig. S12. Correlations between the sizes of pre- and postsynaptic structures.

Proportionalities between the sizes of core structural elements of individual synapses were measured in the CA1sr of fear-conditioned mice. Datasets were categorized based on the history of CA3 neuron activity, as indicated in the legends. (A) Schematic of experience-dependent labeling. (B to G) Correlations between the indicated parameters. Scatter plots with confidence ellipses, sample sizes (n), Spearman correlation coefficients (rs), Fisher transformation scores (z) and p values are shown. (B) Terminal vs. spine head volumes for all synapses. (C) Terminal vs. PSD volumes for all synapses. (E) Terminal vs. spine head volumes in SSB-type synapses. (F) Terminal vs. PSD volumes in SSB-type synapses. (G) Terminal vs. ASI volumes in SSB-type synapses.

All quantifications are from 3 separate mice (7 days post-CFC). Volumetric measurements are displayed in nm<sup>3</sup>.

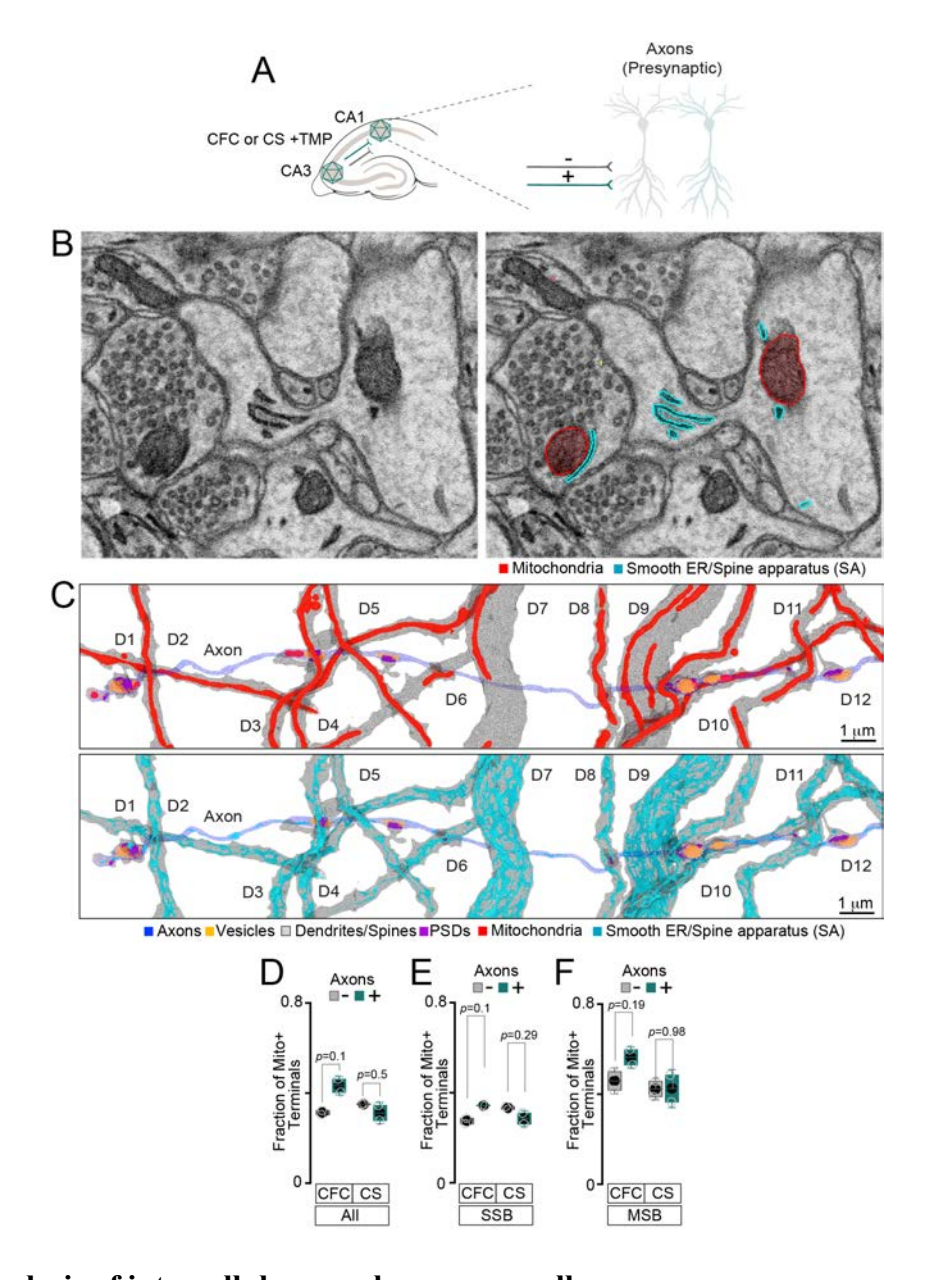


Fig. S13. Analysis of intracellular membrane organelles.

(A) Schematic of experience-dependent labeling and data categorization. (B) Raw 2D images with traced presynaptic mitochondria (red) and postsynaptic spine apparatus (SA, cyan). (C) Reconstructions of mitochondria, smooth endoplasmic reticulum (SER), and SA in SchC axons and/or their target dendrites of PNs in CA1sr. Structures are color-coded as indicated in the legend. (D to E) Fractions of mitochondria-containing terminals formed by Fos/APEX2-mGFP-negative (-) and positive (+) axons of mice subjected to CFC (n = 2) or CS alone (n = 2). (D) All terminals. (E) SSBs. (F) MSBs. p values were calculated using t-tests with Welch correction.

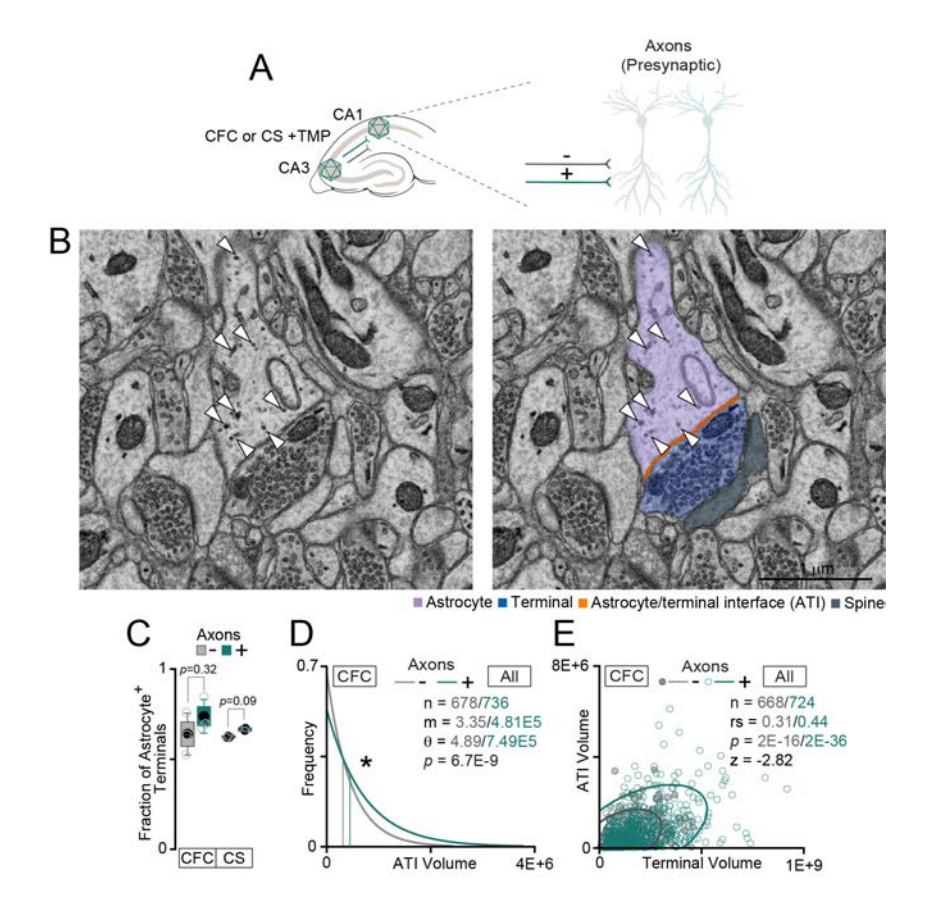


Fig. S14. Interaction between presynaptic terminals and astrocytes.

(A) Schematic of experience-dependent labeling and data categorization. (B) Raw 2D images showing a traced astrocytic process contacting a presynaptic terminal. Structures are color-coded as indicated in the legend. The glycogen deposits are marked by white arrows. (C) Fractions of astrocyte-contacting terminals formed by Fos/APEX2-mGFP-negative (-) and positive (+) axons in mice subjected to CFC (n = 3) or CS alone (n = 2). p values were calculated using a t-test with Welch correction. (D) Distributions of astrocyte/terminal interfaces (ATIs, nm<sup>3</sup>) for (-) and (+) terminals in fear-conditioned mice (n = 3). p value was calculated using a Mann-Whitney test. (E) Correlations between ATI and terminal volumes  $(nm^3)$  for (-) and (+) terminals in fear-conditioned mice CFC (n = 3). Scatter plots with confidence ellipses, sample sizes (n), Spearman correlation coefficients (rs), Fisher transformation scores (z) and p values are shown.

# Data S1

Excel spreadsheets with individual datapoints and quantifications for panels presented in Fig. 1, fig. S3, fig, S4, fig. S6, and fig. S7.

# Data S2

Excel spreadsheets with individual datapoints and quantifications for panels presented in Fig. 2 and fig. S9.

#### Data S3

Excel spreadsheets with individual datapoints and quantifications for panels presented in Fig. 3 and fig. S10.

# Data S4

Excel spreadsheets with individual datapoints and quantifications for panels presented in Fig. 4, Fig 5, and fig. S11.

#### Data S5

Excel spreadsheets with individual datapoints and quantifications for panels presented in Fig. 6, Fig 7, fig. S13, and fig. S14.

#### **References and Notes**

- 1. A. Holtmaat, K. Svoboda, Experience-dependent structural synaptic plasticity in the mammalian brain. *Nat. Rev. Neurosci.* **10**, 647–658 (2009). doi:10.1038/nrn2699 Medline
- 2. S. A. Josselyn, S. Tonegawa, Memory engrams: Recalling the past and imagining the future. *Science* **367**, eaaw4325 (2020). doi:10.1126/science.aaw4325 Medline
- 3. K. P. Berry, E. Nedivi, Spine dynamics: Are they all the same? *Neuron* **96**, 43–55 (2017). doi:10.1016/j.neuron.2017.08.008 Medline
- 4. P. Caroni, F. Donato, D. Muller, Structural plasticity upon learning: Regulation and functions. *Nat. Rev. Neurosci.* **13**, 478–490 (2012). <a href="https://doi.org/10.1038/nrn3258">doi:10.1038/nrn3258</a> Medline
- 5. J. C. Magee, C. Grienberger, Synaptic plasticity forms and functions. *Annu. Rev. Neurosci.* **43**, 95–117 (2020). doi:10.1146/annurev-neuro-090919-022842 Medline
- 6. J. Lisman, Glutamatergic synapses are structurally and biochemically complex because of multiple plasticity processes: Long-term potentiation, long-term depression, short-term potentiation and scaling. *Philos. Trans. R. Soc. Lond. B Biol. Sci.* **372**, 20160260 (2017). doi:10.1098/rstb.2016.0260 Medline
- 7. K. Fox, M. Stryker, Integrating Hebbian and homeostatic plasticity: Introduction. *Philos. Trans. R. Soc. Lond. B Biol. Sci.* **372**, 20160413 (2017). doi:10.1098/rstb.2016.0413 Medline
- 8. L. G. Reijmers, B. L. Perkins, N. Matsuo, M. Mayford, Localization of a stable neural correlate of associative memory. *Science* **317**, 1230–1233 (2007). doi:10.1126/science.1143839 Medline
- 9. X. Liu, S. Ramirez, P. T. Pang, C. B. Puryear, A. Govindarajan, K. Deisseroth, S. Tonegawa, Optogenetic stimulation of a hippocampal engram activates fear memory recall. *Nature* **484**, 381–385 (2012). <a href="https://doi.org/10.1038/nature11028">doi:10.1038/nature11028</a> <a href="https://doi.org/10.1038/nature11028">Medline</a>
- 10. T. Kitamura, S. K. Ogawa, D. S. Roy, T. Okuyama, M. D. Morrissey, L. M. Smith, R. L. Redondo, S. Tonegawa, Engrams and circuits crucial for systems consolidation of a memory. *Science* **356**, 73–78 (2017). doi:10.1126/science.aam6808 Medline
- 11. K. K. Cowansage, T. Shuman, B. C. Dillingham, A. Chang, P. Golshani, M. Mayford, Direct reactivation of a coherent neocortical memory of context. *Neuron* **84**, 432–441 (2014). doi:10.1016/j.neuron.2014.09.022 Medline
- 12. D. S. Roy, Y.-G. Park, M. E. Kim, Y. Zhang, S. K. Ogawa, N. DiNapoli, X. Gu, J. H. Cho, H. Choi, L. Kamentsky, J. Martin, O. Mosto, T. Aida, K. Chung, S. Tonegawa, Brainwide mapping reveals that engrams for a single memory are distributed across multiple brain regions. *Nat. Commun.* **13**, 1799 (2022). <a href="doi:10.1038/s41467-022-29384-4">doi:10.1038/s41467-022-29384-4</a> <a href="Medline">Medline</a>
- 13. L. N. Driscoll, L. Duncker, C. D. Harvey, Representational drift: Emerging theories for continual learning and experimental future directions. *Curr. Opin. Neurobiol.* **76**, 102609 (2022). <a href="https://doi.org/10.1016/j.conb.2022.102609">doi:10.1016/j.conb.2022.102609</a> Medline
- 14. A. Rubin, N. Geva, L. Sheintuch, Y. Ziv, Hippocampal ensemble dynamics timestamp events in long-term memory. *eLife* **4**, e12247 (2015). doi:10.7554/eLife.12247 Medline

- 15. Y. Ziv, L. D. Burns, E. D. Cocker, E. O. Hamel, K. K. Ghosh, L. J. Kitch, A. El Gamal, M. J. Schnitzer, Long-term dynamics of CA1 hippocampal place codes. *Nat. Neurosci.* **16**, 264–266 (2013). <a href="https://doi.org/10.1038/nn.3329">doi:10.1038/nn.3329</a> <a href="https://doi.org/10.1038/nn.3329">Medline</a>
- L. N. Driscoll, N. L. Pettit, M. Minderer, S. N. Chettih, C. D. Harvey, Dynamic reorganization of neuronal activity patterns in parietal cortex. *Cell* 170, 986–999.e16 (2017). doi:10.1016/j.cell.2017.07.021 Medline
- 17. C. E. Schoonover, S. N. Ohashi, R. Axel, A. J. P. Fink, Representational drift in primary olfactory cortex. *Nature* **594**, 541–546 (2021). <a href="https://doi.org/10.1038/s41586-021-03628-7">doi:10.1038/s41586-021-03628-7</a> Medline
- 18. J. S. Lee, J. J. Briguglio, J. D. Cohen, S. Romani, A. K. Lee, The statistical structure of the hippocampal code for space as a function of time, context, and value. *Cell* **183**, 620–635.e22 (2020). doi:10.1016/j.cell.2020.09.024 Medline
- 19. W. Denk, H. Horstmann, Serial block-face scanning electron microscopy to reconstruct three-dimensional tissue nanostructure. *PLOS Biol.* **2**, e329 (2004). doi:10.1371/journal.pbio.0020329 Medline
- N. Kasthuri, K. J. Hayworth, D. R. Berger, R. L. Schalek, J. A. Conchello, S. Knowles-Barley, D. Lee, A. Vázquez-Reina, V. Kaynig, T. R. Jones, M. Roberts, J. L. Morgan, J. C. Tapia, H. S. Seung, W. G. Roncal, J. T. Vogelstein, R. Burns, D. L. Sussman, C. E. Priebe, H. Pfister, J. W. Lichtman, Saturated reconstruction of a volume of neocortex. *Cell* 162, 648–661 (2015). doi:10.1016/j.cell.2015.06.054 Medline
- 21. J. L. Morgan, D. R. Berger, A. W. Wetzel, J. W. Lichtman, The fuzzy logic of network connectivity in mouse visual thalamus. *Cell* **165**, 192–206 (2016). <a href="https://doi.org/10.1016/j.cell.2016.02.033">doi:10.1016/j.cell.2016.02.033</a> <a href="https://doi.org/10.1016/j.cell.2016.02.033">Medline</a>
- 22. M. Helmstaedter, K. L. Briggman, S. C. Turaga, V. Jain, H. S. Seung, W. Denk, Connectomic reconstruction of the inner plexiform layer in the mouse retina. *Nature* **500**, 168–174 (2013). <a href="https://doi.org/10.1038/nature12346">doi:10.1038/nature12346</a> <a href="https://doi.org/10.1038/nature12346">Medline</a>
- 23. F. N. Svara, J. Kornfeld, W. Denk, J. H. Bollmann, Volume EM reconstruction of spinal cord reveals wiring specificity in speed-related motor circuits. *Cell Rep.* **23**, 2942–2954 (2018). doi:10.1016/j.celrep.2018.05.023 Medline
- 24. M. Winding, B. D. Pedigo, C. L. Barnes, H. G. Patsolic, Y. Park, T. Kazimiers, A. Fushiki, I. V. Andrade, A. Khandelwal, J. Valdes-Aleman, F. Li, N. Randel, E. Barsotti, A. Correia, R. D. Fetter, V. Hartenstein, C. E. Priebe, J. T. Vogelstein, A. Cardona, M. Zlatic, The connectome of an insect brain. *Science* 379, eadd9330 (2023). <a href="https://doi.org/10.1126/science.add9330">doi:10.1126/science.add9330</a> Medline
- 25. A. Motta, M. Berning, K. M. Boergens, B. Staffler, M. Beining, S. Loomba, P. Hennig, H. Wissler, M. Helmstaedter, Dense connectomic reconstruction in layer 4 of the somatosensory cortex. *Science* **366**, eaay3134 (2019). <a href="https://doi.org/10.1126/science.aay3134">doi:10.1126/science.aay3134</a> <a href="https://doi.org/10.1126/science.aay3134">Medline</a>
- 26. S. J. Cook, T. A. Jarrell, C. A. Brittin, Y. Wang, A. E. Bloniarz, M. A. Yakovlev, K. C. Q. Nguyen, L. T.-H. Tang, E. A. Bayer, J. S. Duerr, H. E. Bülow, O. Hobert, D. H. Hall, S. W. Emmons, Whole-animal connectomes of both *Caenorhabditis elegans* sexes. *Nature* 571, 63–71 (2019). doi:10.1038/s41586-019-1352-7 Medline

- 27. Y. Mishchenko, T. Hu, J. Spacek, J. Mendenhall, K. M. Harris, D. B. Chklovskii, Ultrastructural analysis of hippocampal neuropil from the connectomics perspective. *Neuron* **67**, 1009–1020 (2010). doi:10.1016/j.neuron.2010.08.014 Medline
- 28. N. L. Turner, T. Macrina, J. A. Bae, R. Yang, A. M. Wilson, C. Schneider-Mizell, K. Lee, R. Lu, J. Wu, A. L. Bodor, A. A. Bleckert, D. Brittain, E. Froudarakis, S. Dorkenwald, F. Collman, N. Kemnitz, D. Ih, W. M. Silversmith, J. Zung, A. Zlateski, I. Tartavull, S. C. Yu, S. Popovych, S. Mu, W. Wong, C. S. Jordan, M. Castro, J. Buchanan, D. J. Bumbarger, M. Takeno, R. Torres, G. Mahalingam, L. Elabbady, Y. Li, E. Cobos, P. Zhou, S. Suckow, L. Becker, L. Paninski, F. Polleux, J. Reimer, A. S. Tolias, R. C. Reid, N. M. da Costa, H. S. Seung, Reconstruction of neocortex: Organelles, compartments, cells, circuits, and activity. *Cell* 185, 1082–1100.e24 (2022). doi:10.1016/j.cell.2022.01.023 Medline
- 29. A. Shapson-Coe, M. Januszewski, D. R. Berger, A. Pope, Y. Wu, T. Blakely, R. L. Schalek, P. H. Li, S. Wang, J. Maitin-Shepard, N. Karlupia, S. Dorkenwald, E. Sjostedt, L. Leavitt, D. Lee, J. Troidl, F. Collman, L. Bailey, A. Fitzmaurice, R. Kar, B. Field, H. Wu, J. Wagner-Carena, D. Aley, J. Lau, Z. Lin, D. Wei, H. Pfister, A. Peleg, V. Jain, J. W. Lichtman, A petavoxel fragment of human cerebral cortex reconstructed at nanoscale resolution. *Science* 384, eadk4858 (2024). doi:10.1126/science.adk4858 Medline
- 30. T. Nakashiba, J. Z. Young, T. J. McHugh, D. L. Buhl, S. Tonegawa, Transgenic inhibition of synaptic transmission reveals role of CA3 output in hippocampal learning. *Science* **319**, 1260–1264 (2008). doi:10.1126/science.1151120 Medline
- 31. S. S. Lam, J. D. Martell, K. J. Kamer, T. J. Deerinck, M. H. Ellisman, V. K. Mootha, A. Y. Ting, Directed evolution of APEX2 for electron microscopy and proximity labeling. *Nat. Methods* **12**, 51–54 (2015). doi:10.1038/nmeth.3179 Medline
- 32. J. D. Martell, T. J. Deerinck, S. S. Lam, M. H. Ellisman, A. Y. Ting, Electron microscopy using the genetically encoded APEX2 tag in cultured mammalian cells. *Nat. Protoc.* **12**, 1792–1816 (2017). <a href="https://doi.org/10.1038/nprot.2017.065">doi:10.1038/nprot.2017.065</a> Medline
- 33. B. Dillingham *et al.*, Fear learning induces long-lasting changes in gene expression and pathway specific presynaptic growth. *BioRxiv.*, (2019).
- 34. R. Sando 3rd, K. Baumgaertel, S. Pieraut, N. Torabi-Rander, T. J. Wandless, M. Mayford, A. Maximov, Inducible control of gene expression with destabilized Cre. *Nat. Methods* **10**, 1085–1088 (2013). <a href="https://doi.org/10.1038/nmeth.2640">doi:10.1038/nmeth.2640</a> <a href="https://doi.org/10.1038/nmeth.2640">Medline</a>
- 35. V. M. A. Carvalho, T. S. Nakahara, M. A. A. Souza, L. M. Cardozo, G. Z. Trintinalia, L. G. Pissinato, J. O. Venancio, L. Stowers, F. Papes, Representation of olfactory information in organized active neural ensembles in the hypothalamus. *Cell Rep.* **32**, 108061 (2020). doi:10.1016/j.celrep.2020.108061 Medline
- 36. E. L. Yap, M. E. Greenberg, Activity-regulated transcription: Bridging the gap between neural activity and behavior. *Neuron* **100**, 330–348 (2018). doi:10.1016/j.neuron.2018.10.013 Medline
- 37. M. Iwamoto, T. Björklund, C. Lundberg, D. Kirik, T. J. Wandless, A general chemical method to regulate protein stability in the mammalian central nervous system. *Chem. Biol.* **17**, 981–988 (2010). doi:10.1016/j.chembiol.2010.07.009 Medline

- 38. C. J. Guenthner, K. Miyamichi, H. H. Yang, H. C. Heller, L. Luo, Permanent genetic access to transiently active neurons via TRAP: Targeted recombination in active populations. *Neuron* **78**, 773–784 (2013). <a href="https://doi.org/10.1016/j.neuron.2013.03.025">doi:10.1016/j.neuron.2013.03.025</a> <a href="https://doi.org/10.1016/j.neuron.2013.03.025">Medline</a>
- 39. L. Ye, W. E. Allen, K. R. Thompson, Q. Tian, B. Hsueh, C. Ramakrishnan, A.-C. Wang, J. H. Jennings, A. Adhikari, C. H. Halpern, I. B. Witten, A. L. Barth, L. Luo, J. A. McNab, K. Deisseroth, Wiring and molecular features of prefrontal ensembles representing distinct experiences. *Cell* 165, 1776–1788 (2016). doi:10.1016/j.cell.2016.05.010 Medline
- 40. S. Tonegawa, M. D. Morrissey, T. Kitamura, The role of engram cells in the systems consolidation of memory. *Nat. Rev. Neurosci.* **19**, 485–498 (2018). doi:10.1038/s41583-018-0031-2 Medline
- 41. J. R. Kremer, D. N. Mastronarde, J. R. McIntosh, Computer visualization of three-dimensional image data using IMOD. *J. Struct. Biol.* **116**, 71–76 (1996). doi:10.1006/jsbi.1996.0013 Medline
- 42. Z. Lin, D. Wei, J. Lichtman, H. Pfister, PyTorch connectomics: A scalable and flexible segmentation framework for em connectomics. <u>arXiv:2112.05754</u> [eess.IV] (2021).
- 43. M. G. Haberl, C. Churas, L. Tindall, D. Boassa, S. Phan, E. A. Bushong, M. Madany, R. Akay, T. J. Deerinck, S. T. Peltier, M. H. Ellisman, CDeep3M-Plug-and-Play cloud-based deep learning for image segmentation. *Nat. Methods* **15**, 677–680 (2018). doi:10.1038/s41592-018-0106-z Medline
- 44. Y. Zhu, M. Uytiepo, E. Bushong, M. Haberl, E. Beutter, F. Scheiwe, W. Zhang, L. Chang, D. Luu, B. Chui, M. Ellisman, A. Maximov, Nanoscale 3D EM reconstructions reveal intrinsic mechanisms of structural diversity of chemical synapses. *Cell Rep.* **35**, 108953 (2021). doi:10.1016/j.celrep.2021.108953 Medline
- 45. G. Buzsáki, K. Mizuseki, The log-dynamic brain: How skewed distributions affect network operations. *Nat. Rev. Neurosci.* **15**, 264–278 (2014). doi:10.1038/nrn3687 Medline
- 46. T. M. Bartol Jr., C. Bromer, J. Kinney, M. A. Chirillo, J. N. Bourne, K. M. Harris, T. J. Sejnowski, Nanoconnectomic upper bound on the variability of synaptic plasticity. *eLife* **4**, e10778 (2015). doi:10.7554/eLife.10778 Medline
- 47. V. A. Alvarez, B. L. Sabatini, Anatomical and physiological plasticity of dendritic spines. *Annu. Rev. Neurosci.* **30**, 79–97 (2007). <a href="https://doi.org/10.1146/annurev.neuro.30.051606.094222">doi:10.1146/annurev.neuro.30.051606.094222</a> <a href="https://doi.org/10.1146/annurev.neuro.30.051606.094222">Medline</a>
- 48. A. Attardo, J. E. Fitzgerald, M. J. Schnitzer, Impermanence of dendritic spines in live adult CA1 hippocampus. *Nature* **523**, 592–596 (2015). doi:10.1038/nature14467 Medline
- 49. F. J. Hwang, R. H. Roth, Y.-W. Wu, Y. Sun, D. K. Kwon, Y. Liu, J. B. Ding, Motor learning selectively strengthens cortical and striatal synapses of motor engram neurons. *Neuron* **110**, 2790–2801.e5 (2022). doi:10.1016/j.neuron.2022.06.006 Medline
- 50. K. E. Sorra, K. M. Harris, Occurrence and three-dimensional structure of multiple synapses between individual radiatum axons and their target pyramidal cells in hippocampal area CA1. *J. Neurosci.* **13**, 3736–3748 (1993). <a href="https://doi.org/10.1523/JNEUROSCI.13-09-03736.1993">doi:10.1523/JNEUROSCI.13-09-03736.1993</a> Medline

- 51. M. Rigby, F. W. Grillo, B. Compans, G. Neves, J. Gallinaro, S. Nashashibi, S. Horton, P. M. Pereira Machado, M. A. Carbajal, G. Vizcay-Barrena, F. Levet, J.-B. Sibarita, A. Kirkland, R. A. Fleck, C. Clopath, J. Burrone, Multi-synaptic boutons are a feature of CA1 hippocampal connections in the stratum oriens. *Cell Rep.* 42, 112397 (2023). doi:10.1016/j.celrep.2023.112397 Medline
- 52. E. B. Bloss, M. S. Cembrowski, B. Karsh, J. Colonell, R. D. Fetter, N. Spruston, Single excitatory axons form clustered synapses onto CA1 pyramidal cell dendrites. *Nat. Neurosci.* **21**, 353–363 (2018). doi:10.1038/s41593-018-0084-6 Medline
- 53. N. Toni, P. A. Buchs, I. Nikonenko, C. R. Bron, D. Muller, LTP promotes formation of multiple spine synapses between a single axon terminal and a dendrite. *Nature* **402**, 421–425 (1999). doi:10.1038/46574 Medline
- 54. Y. Geinisman, R. W. Berry, J. F. Disterhoft, J. M. Power, E. A. Van der Zee, Associative learning elicits the formation of multiple-synapse boutons. *J. Neurosci.* **21**, 5568–5573 (2001). doi:10.1523/JNEUROSCI.21-15-05568.2001 Medline
- 55. N. G. Hedrick, Z. Lu, E. Bushong, S. Singhi, P. Nguyen, Y. Magaña, S. Jilani, B. K. Lim, M. Ellisman, T. Komiyama, Learning binds new inputs into functional synaptic clusters via spinogenesis. *Nat. Neurosci.* **25**, 726–737 (2022). <a href="https://doi.org/10.1038/s41593-022-01086-6">doi:10.1038/s41593-022-01086-6</a> Medline
- 56. Y. Yang, D. Q. Liu, W. Huang, J. Deng, Y. Sun, Y. Zuo, M. M. Poo, Selective synaptic remodeling of amygdalocortical connections associated with fear memory. *Nat. Neurosci.* **19**, 1348–1355 (2016). doi:10.1038/nn.4370 Medline
- 57. J. Liu, J. Qi, X. Chen, Z. Li, B. Hong, H. Ma, G. Li, L. Shen, D. Liu, Y. Kong, H. Zhai, Q. Xie, H. Han, Y. Yang, Fear memory-associated synaptic and mitochondrial changes revealed by deep learning-based processing of electron microscopy data. *Cell Rep.* 40, 111151 (2022). doi:10.1016/j.celrep.2022.111151 Medline
- 58. K. M. Harris, Structural LTP: From synaptogenesis to regulated synapse enlargement and clustering. *Curr. Opin. Neurobiol.* **63**, 189–197 (2020). <a href="doi:10.1016/j.conb.2020.04.009">doi:10.1016/j.conb.2020.04.009</a> Medline
- 59. Y. Hirabayashi, S.-K. Kwon, H. Paek, W. M. Pernice, M. A. Paul, J. Lee, P. Erfani, A. Raczkowski, D. S. Petrey, L. A. Pon, F. Polleux, ER-mitochondria tethering by PDZD8 regulates Ca<sup>2+</sup> dynamics in mammalian neurons. *Science* **358**, 623–630 (2017). doi:10.1126/science.aan6009 Medline
- 60. S. K. Kwon, R. Sando 3rd, T. L. Lewis, Y. Hirabayashi, A. Maximov, F. Polleux, LKB1 regulates mitochondria-dependent presynaptic calcium clearance and neurotransmitter release properties at excitatory synapses along cortical axons. *PLOS Biol.* **14**, e1002516 (2016). doi:10.1371/journal.pbio.1002516 Medline
- 61. M. J. Devine, J. T. Kittler, Mitochondria at the neuronal presynapse in health and disease. *Nat. Rev. Neurosci.* **19**, 63–80 (2018). <a href="https://doi.org/10.1038/nrn.2017.170">doi:10.1038/nrn.2017.170</a> <a href="https://doi.org/10.1038/nrn.2017.170">Medline</a>
- 62. M. Bell, T. Bartol, T. Sejnowski, P. Rangamani, Dendritic spine geometry and spine apparatus organization govern the spatiotemporal dynamics of calcium. *J. Gen. Physiol.* **151**, 1017–1034 (2019). doi:10.1085/jgp.201812261 Medline

- 63. A. Konietzny, S. Wegmann, M. Mikhaylova, The endoplasmic reticulum puts a new spin on synaptic tagging. *Trends Neurosci.* **46**, 32–44 (2023). <a href="doi:10.1016/j.tins.2022.10.012">doi:10.1016/j.tins.2022.10.012</a> Medline
- 64. H. L. Smith, J. N. Bourne, G. Cao, M. A. Chirillo, L. E. Ostroff, D. J. Watson, K. M. Harris, Mitochondrial support of persistent presynaptic vesicle mobilization with age-dependent synaptic growth after LTP. *eLife* 5, e15275 (2016). doi:10.7554/eLife.15275 Medline
- 65. A. Maximov, T. C. Südhof, Autonomous function of synaptotagmin 1 in triggering synchronous release independent of asynchronous release. *Neuron* **48**, 547–554 (2005). doi:10.1016/j.neuron.2005.09.006 Medline
- 66. T. L. Lewis Jr., S. K. Kwon, A. Lee, R. Shaw, F. Polleux, MFF-dependent mitochondrial fission regulates presynaptic release and axon branching by limiting axonal mitochondria size. *Nat. Commun.* **9**, 5008 (2018). <a href="https://doi.org/10.1038/s41467-018-07416-2">doi:10.1038/s41467-018-07416-2</a> <a href="https://doi.org/10.1038/s41467-018-07416-2">Medline</a>
- 67. N. J. Allen, C. Eroglu, Cell biology of astrocyte-synapse interactions. *Neuron* **96**, 697–708 (2017). doi:10.1016/j.neuron.2017.09.056 Medline
- 68. B. S. Khakh, M. V. Sofroniew, Diversity of astrocyte functions and phenotypes in neural circuits. *Nat. Neurosci.* **18**, 942–952 (2015). doi:10.1038/nn.4043 Medline
- 69. A. Kol, A. Adamsky, M. Groysman, T. Kreisel, M. London, I. Goshen, Astrocytes contribute to remote memory formation by modulating hippocampal-cortical communication during learning. *Nat. Neurosci.* **23**, 1229–1239 (2020). <a href="mailto:doi:10.1038/s41593-020-0679-6">doi:10.1038/s41593-020-0679-6</a> Medline
- 70. W. Sun, Z. Liu, X. Jiang, M. B. Chen, H. Dong, J. Liu, T. C. Südhof, S. R. Quake, Spatial transcriptomics reveal neuron-astrocyte synergy in long-term memory. *Nature* **627**, 374–381 (2024). doi:10.1038/s41586-023-07011-6 Medline
- 71. M. B. Chen, X. Jiang, S. R. Quake, T. C. Südhof, Persistent transcriptional programmes are associated with remote memory. *Nature* **587**, 437–442 (2020). <a href="https://doi.org/10.1038/s41586-020-2905-5">doi:10.1038/s41586-020-2905-5</a> <a href="https://doi.org/10.1038/s41586-020-2905-5">Medline</a>
- 72. A. Maximov, O. H. Shin, X. Liu, T. C. Südhof, Synaptotagmin-12, a synaptic vesicle phosphoprotein that modulates spontaneous neurotransmitter release. *J. Cell Biol.* **176**, 113–124 (2007). doi:10.1083/jcb.200607021 Medline
- 73. R. L. Redondo, R. G. Morris, Making memories last: The synaptic tagging and capture hypothesis. *Nat. Rev. Neurosci.* **12**, 17–30 (2011). <a href="https://doi.org/10.1038/nrn2963">doi:10.1038/nrn2963</a> <a href="https://doi.org/10.1038/nrn2963">Medline</a>
- 74. T. Rogerson, D. J. Cai, A. Frank, Y. Sano, J. Shobe, M. F. Lopez-Aranda, A. J. Silva, Synaptic tagging during memory allocation. *Nat. Rev. Neurosci.* **15**, 157–169 (2014). <a href="https://doi.org/10.1038/nrn3667">doi:10.1038/nrn3667</a> Medline
- 75. N. Matsuo, L. Reijmers, M. Mayford, Spine-type-specific recruitment of newly synthesized AMPA receptors with learning. *Science* **319**, 1104–1107 (2008). doi:10.1126/science.1149967 Medline
- 76. J. H. Choi, S.-E. Sim, J. I. Kim, D. I. Choi, J. Oh, S. Ye, J. Lee, T. Kim, H.-G. Ko, C.-S. Lim, B.-K. Kaang, Interregional synaptic maps among engram cells underlie memory formation. *Science* **360**, 430–435 (2018). <a href="https://doi.org/10.1126/science.aas9204">doi:10.1126/science.aas9204</a> <a href="https://doi.org/10.1126/science.aas9204">Medline</a>
- 77. B. Wamsley, G. Fishell, Genetic and activity-dependent mechanisms underlying interneuron diversity. *Nat. Rev. Neurosci.* **18**, 299–309 (2017). <a href="https://doi.org/10.1038/nrn.2017.30">doi:10.1038/nrn.2017.30</a> <a href="https://doi.org/10.1038/nrn.2017.30">Medline</a>

- 78. D. L. Hunt, D. Linaro, B. Si, S. Romani, N. Spruston, A novel pyramidal cell type promotes sharp-wave synchronization in the hippocampus. *Nat. Neurosci.* **21**, 985–995 (2018). doi:10.1038/s41593-018-0172-7 Medline
- 79. Z. Yao, C. T. J. van Velthoven, M. Kunst, M. Zhang, D. McMillen, C. Lee, W. Jung, J. Goldy, A. Abdelhak, M. Aitken, K. Baker, P. Baker, E. Barkan, D. Bertagnolli, A. Bhandiwad, C. Bielstein, P. Bishwakarma, J. Campos, D. Carey, T. Casper, A. B. Chakka, R. Chakrabarty, S. Chavan, M. Chen, M. Clark, J. Close, K. Crichton, S. Daniel, P. DiValentin, T. Dolbeare, L. Ellingwood, E. Fiabane, T. Fliss, J. Gee, J. Gerstenberger, A. Glandon, J. Gloe, J. Gould, J. Gray, N. Guilford, J. Guzman, D. Hirschstein, W. Ho, M. Hooper, M. Huang, M. Hupp, K. Jin, M. Kroll, K. Lathia, A. Leon, S. Li, B. Long, Z. Madigan, J. Malloy, J. Malone, Z. Maltzer, N. Martin, R. McCue, R. McGinty, N. Mei, J. Melchor, E. Meyerdierks, T. Mollenkopf, S. Moonsman, T. N. Nguyen, S. Otto, T. Pham, C. Rimorin, A. Ruiz, R. Sanchez, L. Sawyer, N. Shapovalova, N. Shepard, C. Slaughterbeck, J. Sulc, M. Tieu, A. Torkelson, H. Tung, N. Valera Cuevas, S. Vance, K. Wadhwani, K. Ward, B. Levi, C. Farrell, R. Young, B. Staats, M. M. Wang, C. L. Thompson, S. Mufti, C. M. Pagan, L. Kruse, N. Dee, S. M. Sunkin, L. Esposito, M. J. Hawrylycz, J. Waters, L. Ng, K. Smith, B. Tasic, X. Zhuang, H. Zeng, A high-resolution transcriptomic and spatial atlas of cell types in the whole mouse brain. *Nature* **624**, 317– 332 (2023). doi:10.1038/s41586-023-06812-z Medline
- 80. M. Zhang, X. Pan, W. Jung, A. R. Halpern, S. W. Eichhorn, Z. Lei, L. Cohen, K. A. Smith, B. Tasic, Z. Yao, H. Zeng, X. Zhuang, Molecularly defined and spatially resolved cell atlas of the whole mouse brain. *Nature* **624**, 343–354 (2023). <a href="https://doi.org/10.1038/s41586-023-06808-9">doi:10.1038/s41586-023-06808-9</a> Medline
- 81. Z. Yao, C. T. J. van Velthoven, T. N. Nguyen, J. Goldy, A. E. Sedeno-Cortes, F. Baftizadeh, D. Bertagnolli, T. Casper, M. Chiang, K. Crichton, S.-L. Ding, O. Fong, E. Garren, A. Glandon, N. W. Gouwens, J. Gray, L. T. Graybuck, M. J. Hawrylycz, D. Hirschstein, M. Kroll, K. Lathia, C. Lee, B. Levi, D. McMillen, S. Mok, T. Pham, Q. Ren, C. Rimorin, N. Shapovalova, J. Sulc, S. M. Sunkin, M. Tieu, A. Torkelson, H. Tung, K. Ward, N. Dee, K. A. Smith, B. Tasic, H. Zeng, A taxonomy of transcriptomic cell types across the isocortex and hippocampal formation. *Cell* **184**, 3222–3241.e26 (2021). doi:10.1016/j.cell.2021.04.021 Medline
- 82. D. J. Cai, D. Aharoni, T. Shuman, J. Shobe, J. Biane, W. Song, B. Wei, M. Veshkini, M. La-Vu, J. Lou, S. E. Flores, I. Kim, Y. Sano, M. Zhou, K. Baumgaertel, A. Lavi, M. Kamata, M. Tuszynski, M. Mayford, P. Golshani, A. J. Silva, A shared neural ensemble links distinct contextual memories encoded close in time. *Nature* **534**, 115–118 (2016). <a href="https://doi.org/10.1038/nature17955">doi:10.1038/nature17955</a> <a href="https://doi.org/10.1038/nature17955">Medline</a>
- 83. M. Pignatelli, T. J. Ryan, D. S. Roy, C. Lovett, L. M. Smith, S. Muralidhar, S. Tonegawa, Engram Cell Excitability State Determines the Efficacy of Memory Retrieval. *Neuron* **101**, 274–284.e5 (2019). doi:10.1016/j.neuron.2018.11.029 Medline
- 84. A. J. Mocle, A. I. Ramsaran, A. D. Jacob, A. J. Rashid, A. Luchetti, L. M. Tran, B. A. Richards, P. W. Frankland, S. A. Josselyn, Excitability mediates allocation of preconfigured ensembles to a hippocampal engram supporting contextual conditioned threat in mice. *Neuron* **112**, 1487–1497.e6 (2024). <a href="https://doi.org/10.1016/j.neuron.2024.02.007">doi:10.1016/j.neuron.2024.02.007</a> <a href="https://doi.org/10.1016/j.neuron.2024.02.007">Medline</a>

- 85. I. Soltesz, A. Losonczy, CA1 pyramidal cell diversity enabling parallel information processing in the hippocampus. *Nat. Neurosci.* **21**, 484–493 (2018). <a href="https://doi.org/10.1038/s41593-018-0118-0">doi:10.1038/s41593-018-0118-0</a> <a href="https://doi.org/10.1038/s41593-018-0118-0">Medline</a>
- 86. M. S. Cembrowski, N. Spruston, Heterogeneity within classical cell types is the rule: Lessons from hippocampal pyramidal neurons. *Nat. Rev. Neurosci.* **20**, 193–204 (2019). doi:10.1038/s41583-019-0125-5 Medline
- 87. J. C. Jimenez, J. E. Berry, S. C. Lim, S. K. Ong, M. A. Kheirbek, R. Hen, Contextual fear memory retrieval by correlated ensembles of ventral CA1 neurons. *Nat. Commun.* **11**, 3492 (2020). <a href="https://doi.org/10.1038/s41467-020-17270-w">doi:10.1038/s41467-020-17270-w</a> Medline
- 88. L. Luo, E. M. Callaway, K. Svoboda, Genetic dissection of neural circuits: A decade of progress. *Neuron* **98**, 865 (2018). doi:10.1016/j.neuron.2018.05.004 Medline
- 89. T. C. Südhof, Towards an understanding of synapse formation. *Neuron* **100**, 276–293 (2018). doi:10.1016/j.neuron.2018.09.040 Medline
- 90. Y. Zhu, M. Huang, E. Bushong, S. Phan, M. Uytiepo, E. Beutter, D. Boemer, K. Tsui, M. Ellisman, A. Maximov, Class IIa HDACs regulate learning and memory through dynamic experience-dependent repression of transcription. *Nat. Commun.* **10**, 3469 (2019). doi:10.1038/s41467-019-11409-0 Medline
- 91. S. Pieraut, N. Gounko, R. Sando 3rd, W. Dang, E. Rebboah, S. Panda, L. Madisen, H. Zeng, A. Maximov, Experience-dependent remodeling of basket cell networks in the dentate gyrus. *Neuron* 84, 107–122 (2014). <a href="https://doi.org/10.1016/j.neuron.2014.09.012">doi:10.1016/j.neuron.2014.09.012</a> Medline
- 92. R. Sando, E. Bushong, Y. Zhu, M. Huang, C. Considine, S. Phan, S. Ju, M. Uytiepo, M. Ellisman, A. Maximov, Assembly of excitatory synapses in the absence of glutamatergic neurotransmission. *Neuron* **94**, 312–321.e3 (2017). <a href="https://doi.org/doi:10.1016/j.neuron.2017.03.047">doi:10.1016/j.neuron.2017.03.047</a>
  <a href="https://doi.org/d
- 93. M. Huang, S. Pieraut, J. Cao, F. de Souza Polli, V. Roncace, G. Shen, C. Ramos-Medina, H. Lee, A. Maximov, Nr4a1 regulates cell-specific transcriptional programs in inhibitory GABAergic interneurons. *Neuron* **112**, 2031–2044.e7 (2024). doi:10.1016/j.neuron.2024.03.018 Medline
- 94. Y. Shinohara, K. Kohara, Projections of hippocampal CA2 pyramidal neurons: Distinct innervation patterns of CA2 compared to CA3 in rodents. *Hippocampus* **33**, 691–699 (2023). doi:10.1002/hipo.23519 Medline
- 95. J. Schindelin, I. Arganda-Carreras, E. Frise, V. Kaynig, M. Longair, T. Pietzsch, S. Preibisch, C. Rueden, S. Saalfeld, B. Schmid, J.-Y. Tinevez, D. J. White, V. Hartenstein, K. Eliceiri, P. Tomancak, A. Cardona, Fiji: An open-source platform for biological-image analysis. *Nat. Methods* **9**, 676–682 (2012). <a href="https://doi.org/10.1038/nmeth.2019">doi:10.1038/nmeth.2019</a> <a href="https://doi.org/10.1038/nmeth.2019">Medline</a>
- 96. D. R. Berger, H. S. Seung, J. W. Lichtman, VAST (Volume Annotation and Segmentation Tool): Efficient manual and semi-automatic labeling of large 3D image stacks. *Front. Neural Circuits* **12**, 88 (2018). <a href="https://doi.org/10.3389/fncir.2018.00088">doi:10.3389/fncir.2018.00088</a> <a href="https://doi.org/10.3389/fncir.2018.00088">Medline</a>
- 97. I. Spiegel, A. R. Mardinly, H. W. Gabel, J. E. Bazinet, C. H. Couch, C. P. Tzeng, D. A. Harmin, M. E. Greenberg, Npas4 regulates excitatory-inhibitory balance within neural circuits through cell-type-specific gene programs. *Cell* **157**, 1216–1229 (2014). <a href="https://doi.org/10.1016/j.cell.2014.03.058">doi:10.1016/j.cell.2014.03.058</a> Medline

- 98. W. C. Risher, T. Ustunkaya, J. Singh Alvarado, C. Eroglu, Rapid Golgi analysis method for efficient and unbiased classification of dendritic spines. *PLOS ONE* **9**, e107591 (2014). doi:10.1371/journal.pone.0107591 Medline
- 99. A. M. Mood, F. A. Graybill, D. C. Boes, *Introduction to the Theory of Statistics: McGraw-Hill Series in Probability and Statistics* (McGraw-Hill, ed. 3, 1973).